Equilibrium barium isotope fractionation between minerals and aqueous solution from first-principles calculations

Wenzhong Wang[a, b, *], Zhongqing Wu[a, d], Fang Huang[c, d]

[a]Laboratory of Seismology and Physics of Earth's Interior, School of Earth and Space Sciences, University of Science and Technology of China, Hefei, Anhui 230026, China

[b]Department of Earth Sciences, University College London, London WC1E 6BT, United Kingdom

[c]CAS Key Laboratory of Crust-Mantle Materials and Environments, School of Earth and Space Sciences, University of Science and Technology of China, Hefei, Anhui 230026, China

[d]CAS Center for Excellence in Comparative Planetology, USTC, Hefei, Anhui 230026, China

[*]Corresponding author: Wenzhong Wang (wenzhong.wang@ucl.ac.uk)

Abstract

Barium isotopes could be a novel tracer in low-temperature geochemical processes such as the Ba cycle in rivers and oceans. Equilibrium Ba isotope fractionation between Ba-hosting minerals and aqueous solution is of great importance for the applications of Ba isotopes in geochemistry, but it remains poorly constrained. In this study, we performed first-principles calculations based on the density functional theory (DFT) to determine the equilibrium Ba isotope fractionation between minerals and aqueous solution ($10^3\ln\alpha_{mineral\text{-}Ba\_aq}$ of $^{137}Ba/^{134}Ba$). The structural properties of aqueous Ba^{2+} are well predicted by the first-principles molecular dynamics (FPMD) simulation and 121 snapshots are extracted from FPMD trajectories to estimate the reduced partition function ratio (β factor or $10^3\ln\beta$ of $^{137}Ba/^{134}Ba$) of aqueous Ba^{2+}. The $10^3\ln\beta$ decreases in the sequence of aragonite > calcite > aqueous Ba^{2+} ~ witherite > barite. The β factor is dominantly determined by the force constant, which is affected by both the average Ba-O bond length and the coordination number.

Our results show that $10^3\ln\alpha_{aragonite\text{-}Ba\_aq}$ and $10^3\ln\alpha_{witherite\text{-}Ba\_aq}$ are 0.36‰ and -0.02‰ at 300 K, respectively, consistent with results of experimental studies at equilibrium. The depletion of heavy Ba isotopes observed in natural corals relative to seawater suggests that kinetic effects play an important role in Ba isotope fractionation during coral growth. The $10^3\ln\alpha_{barite\text{-}Ba\_aq}$ is only -0.17‰ at 300 K, indicating limited Ba isotope fractionation caused by the Ba removal stemmed from inorganic barite precipitation. Overall, the equilibrium Ba isotope fractionation factors between minerals and aqueous Ba^{2+} calculated in this study provide a guideline for applications of Ba isotopes in low-temperature geochemistry.

Keywords: Ba isotopes; Equilibrium fractionation; Density functional theory; First-principles molecular dynamics simulations; Ba cycle; barite; carbonates

1. Introduction

Barium (Ba) is a relatively refractory element belonging to the group of alkali-

earth metals. Because Ba is highly incompatible during mantle melting, it is mostly concentrated in the Earth's crust and crustal-derived sediments but strongly depleted in the mantle (Sun and McDonough, 1989; Salters and Stracke, 2004; Gonneea and Paytan, 2006; Rudnick and Gao, 2014). The concentration ratio of Ba between the crust and the mantle is about 100. As such, Ba could be potentially used to trace the recycling of crustal materials into the convective mantle. Meanwhile, Ba is also a highly fluid-mobile element (Kessel et al., 2005; Carter et al., 2015) and was observed to be enriched in arc magmas (e.g., Elliott et al., 1997), making it a powerful indicator of fluid activities in the slabs. In marine geochemistry, Ba in shallow-water corals has also been applied to trace changes in the seawater Ba concentrations driven by riverine inputs, upwelling, and productivity (Lea et al., 1989; McCulloch et al., 2003; Montaggioni et al., 2006; Alibert and Kinsley, 2008; Moyer et al., 2012; LaVigne et al., 2016; Lewis et al., 2018). The Ba accumulation in marine sediments is thought to be a potential proxy for export production in the oceans (Eagle et al., 2003; Paytan and Griffith, 2007; Shen et al., 2015).

Barium has seven stable isotopes, ^{130}Ba (0.11%), ^{132}Ba (0.10%), ^{134}Ba (2.42%), ^{135}Ba (6.59%), ^{136}Ba (7.85%), ^{137}Ba (11.23%), and ^{138}Ba (71.70%). With the advancement in analytical techniques, Ba isotope compositions ($\delta^{x/134}Ba_{sample}$ = $[(^{x}Ba/^{134}Ba)_{sample}/(^{x}Ba/^{134}Ba)_{SRM3104a} -1] \times 1000$ (‰), where x is 137 or 138, and SRM3104a is the Ba standard solution) of different samples can be measured with the analytical uncertainty of 0.04‰ (Nan et al., 2018; Zeng et al., 2019; Liu et al., 2019; Li et al., 2020). The $\delta^{138/134}$Ba of natural samples have been reported to vary in a wide range (-0.8-+1.3‰) as summarized in Charbonnier et al. (2018), implying that Ba isotopes could be an important tracer in marine and mantle geochemistry (Horner et al., 2015; Nielsen et al., 2018; Nielsen et al., 2020). Indeed, Ba isotopes have been increasingly used to investigate the cycling of Ba in the oceans including riverine inputs, the Ba removal and/or utilization during biochemical processes, and the oceanic water-mass circulation (Horner et al., 2015; Cao et al., 2016; Bates et al., 2017; Hsieh and

Henderson, 2017; Bridgestock et al., 2018; Gou et al., 2020). These studies demonstrate a strong negative correlation between $\delta^{137/134}$Ba and Ba concentration, suggesting that barite precipitation may be important to resolve the vertical Ba isotope distributions in the oceans (Horner et al., 2015; Bates et al., 2017; Hsieh and Henderson, 2017; Bridgestock et al., 2018).

Understanding the Ba isotope fractionation mechanisms is critical for the applications of Ba isotopes in marine geochemistry. The most common naturally occurring minerals of Ba are barite and witherite, and some carbonates are also important hosts for Ba. Significant effort has been expanded to constrain the Ba isotope fractionation between major Ba-bearing minerals and aqueous solution, but there are still some discrepancies between different studies. Particularly, previous experimental studies (von Allmen et al., 2010; Böttcher et al., 2018) have investigated the Ba isotope fractionation between barite/witherite and aqueous solution by performing precipitation and/or dissolution experiments at 294-333 K and found that both barite and witherite are depleted in heavy Ba isotopes relative to aqueous solution. However, Mavromatis et al. (2016) did not observe significant Ba isotope fractionation between witherite and aqueous solution in their precipitation and dissolution experiments at 298 K. Recently, Mavromatis et al. (2020) performed inorganic precipitation experiments at 298 K to calibrate the Ba isotope fractionation between calcite/aragonite and aqueous solution ($\Delta^{137/134}Ba_{calcite/aragonite\text{-}solution}$). Their results show that $\Delta^{137/134}Ba_{aragonite\text{-}solution}$ systematically decreases as a function of increasing aragonite growth rate, but $\Delta^{137/134}Ba_{calcite\text{-}solution}$ does not exhibit a significant variation with the calcite growth rate. Using a simplified model of transition state theory to fit data, they inferred that no significant Ba isotope fractionation occurs between calcite and aqueous solution at 298 K, while $\Delta^{137/134}Ba_{aragonite\text{-}solution}$ is up to +0.27‰ at equilibrium. Their theoretical calculations, however, suggest that at equilibrium both calcite and aragonite should be enriched in heavy isotopes relative to aqueous Ba^{2+} that was represented by barium hydroxide octahydrate. Collectively, the equilibrium Ba isotope fractionation between

these minerals and aqueous solution has not been well understood. One of the most important concerns with these experiments is that it is difficult to achieve Ba isotopic exchange equilibrium between two phases at low temperatures.

In this study, we performed first-principles calculations based on the density functional theory (DFT) to determine the equilibrium Ba isotope fractionation between multiple minerals and aqueous solution. The atoms in solids are bound tightly to each other which makes it resistant to change, whereas those in liquids are free to move around to maintain dynamic positions. Similar to previous studies (Méheut et al., 2009; Schauble, 2011; Huang et al., 2013, 2014; Feng et al., 2014; Wang et al., 2017a, b; Li et al., 2019a, b), the equilibrium Ba isotope fractionation between different minerals were calculated from vibrational frequencies based on the DFT with the periodic boundary conditions. For aqueous Ba^{2+}, we performed first-principles molecular dynamics (FPMD) simulation to obtain its structural properties and then extracted an adequately large number of snapshots from the FPMD trajectories for the β-factor calculations (Kowalski et al., 2013; Ducher et al., 2018; Wang et al., 2019). We further compared our results with previous experimental measurements and discussed the Ba isotope fractionation behaviors with respect to low-temperature geochemical processes.

2. Methods

2.1 Equilibrium mass-dependent isotope fractionation

Equilibrium isotope fractionation arises from changes in vibrational frequencies caused by the isotopic substitution of an element in a given system (Bigeleisen and Mayer, 1947; Urey, 1947). Following Bigeleisen and Mayer (1947), the reduced partition function ratio β_A of an element X in Phase A can be calculated from:

$$\beta_A = \frac{Q_h}{Q_l} = \prod_i^{3N} \frac{u_{ih}}{u_{il}} \frac{e^{-\frac{1}{2}u_{ih}}}{1-e^{-u_{ih}}} \frac{1-e^{-u_{il}}}{e^{-\frac{1}{2}u_{il}}} \quad (1)$$

where h and l represent the heavy and light isotopes, respectively; i is a running index of vibrational frequency mode, and N is the number of atoms in the unit cell; Q_h and Q_l refer to the vibrational partition function for the heavy and light isotopes, respectively.

Parameters u_{ih} and u_{il} are defined as:

$$u_{ih\ or\ il} = \hbar\nu_{ih\ or\ il}/k_B T \tag{2}$$

where $\hbar$ and k_B are the Planck and Boltzmann constants, respectively; T is the temperature in Kelvin, and $\nu_{ih\ or\ il}$ is the vibrational frequency of the ith mode. The β-factor of Phase A is also the equilibrium isotope fractionation factor between Phase A and an ideal gas of X atoms. Following Richet et al. (1977), the equilibrium isotope fractionation between two Phases A and B can be derived in per mil (‰) as:

$$\Delta_{A-B} \approx 10^3 ln\alpha_{A-B} = 10^3 ln\beta_A - 10^3 ln\beta_B \tag{3}$$

2.2 The single-atom approximation

According to Bigeleisen and Mayer (1947) and Kowalski et al. (2013), for small $\Delta u_i = u_{il} - u_{ih}$ Eq. (1) can be written as:

$$\beta = 1 + \sum_{i=1}^{3N} \left(\frac{1}{2} - \frac{1}{u_i} + \frac{1}{exp(u_i)-1}\right) \Delta u_i \tag{4}$$

The Taylor expansion of the function enclosed by the summation sign is:

$$G(u_i) = \frac{1}{2} - \frac{1}{u_i} + \frac{1}{\exp(u_i)-1} = \frac{u_i}{12} - \frac{{u_i}^3}{720} + \frac{{u_i}^5}{30240} - \frac{{u_i}^7}{1209600} + \cdots \tag{5}$$

When the first term of the Taylor expansion is considered, the β factor is:

$$\beta = 1 + \sum_{i=1}^{3N} \frac{u_i}{12} \Delta u_i = 1 + \sum_{i=1}^{3N} \frac{{u_{il}}^2 - {u_{ih}}^2}{24} \tag{6}$$

As we only consider changes in vibrational frequencies caused by the isotopic substitution of the element of interest, Eq. (6) can be expressed as:

$$\beta = 1 + \sum_{i=1}^{3N} \frac{{u_{il}}^2 - {u_{ih}}^2}{24} = 1 + \left(\frac{1}{m_l} - \frac{1}{m_h}\right) \frac{\hbar^2}{24{k_B}^2 T^2} \sum_{i=1}^{3} A_i$$

$$= 1 + \left(\frac{1}{m_l} - \frac{1}{m_h}\right) \frac{\hbar^2}{8{k_B}^2 T^2} < F > \tag{7}$$

where m_l and m_h are the mass of light and heavy isotopes, respectively. A_i $(i = 1, 2, 3)$ are the force constants acting on the isotopic atom in the three perpendicular spatial directions, and <F> is the average force constant. The use of Eq. (7) requires the validity criteria that frequencies related to the element of interest ω_i (cm^{-1}) ≤ 1.39 T (T is the temperature in Kelvin).

2.3 First-principles calculations

We performed first-principles calculations based on the density functional theory (DFT) using VASP with the projector-augmented wave (PAW) method (Blöchl, 1994). The generalized-gradient approximation (GGA) (Perdew et al., 1996) for the exchange-correlation functional was adopted and the PAW-PBE pseudopotentials were used. For solid phases, their cell parameters and atomic positions were optimized at ambient pressure with a k-point grid mesh that depends on the unit-cell sizes (Table S1). The residual forces converge within 10^{-3} eV/Å and the energy cutoff was 600 eV. Then we calculated phonon frequencies of all relaxed structures using the finite displacement method as implemented in the open-source code PHONOPY (Togo and Tanaka, 2015), and the β factors of $^{137}Ba/^{134}Ba$ can be obtained using Eq. (1).

In order to obtain the structure of aqueous Ba^{2+}, we performed first-principles molecular dynamic simulations using VASP based on a cubic cell containing one Ba atom, two Cl atoms, and 70 water molecules ($BaCl_2(H_2O)_{70}$). Van der Waals interactions in aqueous solution were taken into account using the D2 method (Montanari et al., 2006). The FPMD simulation was performed in the NVT thermodynamic ensemble with a fixed temperature of 300 K and the Nosé thermostat was used. The cell parameter of the cubic box is 12.845 Å, which gives a simulated statistical pressure of approximately zero kbar. The time step was set to be 1 fs, and the total running time is up to 45 ps. The Brillouin zone summations over the electronic states were performed at gamma point. After equilibration, we extracted 121 snapshots from the FPMD trajectory every 250 steps and only optimized the atomic positions of Ba with fixed cubic boxes. This strategy makes the Ba atom in each snapshot move to the local equilibrium positions and the force constant matrix of Ba atom can be calculated from the small displacement method based on the harmonic approximation. Although the Ba atomic positions have been slightly changed compared to the initial structure, the single-atom relaxation does not change the positions of other atoms around the Ba atom, suggesting that most structural information in the initial snapshots is unreservedly inherited. The force constant of the Ba atom in aqueous solution is

the cumulative average in the time domain. The β factor of aqueous Ba^{2+} can be obtained from the force constant <F> using Eq. (7). The reliability and validity of this method will be discussed in section 3.3.

In order to check the nuclear volume effect (NVE) on the Ba isotope fractionation, we calculated the total energies of Ba^{2+} ion and Ba^0 atom using all-electron Dirac-Hartree-Fock (DHF) theory with four-component wave functions by DIRAC software package by following the computational procedure in Yang and Liu (2015). Ba^{2+} and Ba^0 are both closed-shell species with the electron configurations of [Xe] and [Xe]$6s^2$, respectively. "Double-zeta" basis sets were used for Ba^{2+} ion and Ba^0 atom. Total energies of different isotopologues were obtained by Gaussian exponent ξ ($\xi=3/2\langle r^2\rangle$, where $\langle r^2\rangle$ are the mean square nuclear charge radii from Angeli (2004)). The results show that the equilibrium NVE-driving $^{137}Ba/^{134}Ba$ isotope fractionation between Ba^{2+} and Ba^0 is negligible (~0.02 ‰ at 300 K), suggesting that the NVE for Ba isotopes is insignificant.

3. Results

3.1 Structures of Ba-bearing minerals and aqueous Ba^{2+}

The minerals investigated in this study include barite, witherite, Ba-doped aragonite and calcite, $BaCl_2$, $Ba(NO_3)_2$, phosphates ($Ba(PO_3)_2$, $Ba_3(PO_4)_2$, $BaHPO_4$, and $Ba(H_2PO_4)_2$), and barium hydroxide octahydrate ($Ba(OH)_2H_2O$, $Ba(OH)_2(H_2O)_3$, and $Ba(OH)_2(H_2O)_8$). Barium is a trace element in aragonite and calcite. Previous FPMD simulations and X-ray absorption spectroscopy measurements on calcite demonstrated that Ba incorporates in calcite via substitution in the Ca site (Reeder et al., 1999; Kerisit and Prange, 2019). Although there is no available data for Ba in aragonite, Ba likely substitutes for Ca in aragonite due to similar ionic radii. Thus, similar to our previous works (Wang et al., 2017a, b, 2019), we constructed the initial structures of Ba-doped aragonite and calcite with different Ba concentrations by replacing one Ca atom with one Ba atom in their supercells that can be generated

by expanding the conventional cell along with different directions. For instance, we substituted one Ba atom with one Ca atom in 160-atom (2×2×2) and 240-atom (3×2×2) aragonite supercells to generate the Ba-doped structures with Ba/(Ba+Ca) ratio of 1/32 and 1/48, respectively.

The relaxed structures of solid phases are shown in Fig. S1 and their cell parameters and volumes are reported in Table S1. The GGA calculations predict larger volumes for all solid phases except $Ba(OH)_2(H_2O)_8$ than experimental measurements (Table S1). The calculated volume of $Ba(OH)_2(H_2O)_8$ is about 0.6% smaller than the experimental data. Except for $Ba(OH)_2(H_2O)_8$, the volume differences between our GGA calculations and experimental data range from 1.3% for $Ba(OH)_2(H_2O)_3$ to 6.1% for $Ba(H_2PO_4)_2$, with an average difference of 4.2%. Typically, the GGA overestimates but the local density approximation (LDA) underestimates the equilibrium mineral volumes (Wentzcovitch et al., 2010; Schauble, 2011; Wang et al., 2017a, 2019; Wang and Wu, 2018). The calculated vibrational frequencies of witherite and barite are compared with experimental measurements in Fig. S2, which shows good agreement between theoretical and experimental data with a slope of 1.018±0.01. Following the analyses in Méheut et al. (2009), a systematic correction of n% on the phonon frequencies induces a relative systematic correction of n% on the $10^3\ln\beta$ at low temperatures. Thus, the relative uncertainty of $10^3\ln\beta$ calculated in this study is about 3%. Following the rule of relative error propagation $\Delta E = \sqrt{\sum_A (\frac{\partial E}{\partial A})^2 (\Delta A)^2}$, where ΔE and ΔA are the relative errors of $10^3\ln\alpha$ and $10^3\ln\beta$, respectively, the relative error of $10^3\ln\alpha$ between two minerals is about 4%.

3.2 Average Ba-O/Cl bond lengths

The average Ba-O/Cl (Ba-Cl bond in $BaCl_2$) bond lengths and the coordination numbers (CNs) in all solid phases are listed in Table 1. The cutoff for Ba-O/Cl bond lengths will affect the calculations of average bond lengths and CNs. The Ba-Cl bond lengths in $BaCl_2$ range from 3.12 Å to 3.27 Å, which are longer than most Ba-O bond lengths in other minerals. As such, we adopted the cutoff of 3.3 Å for all Ba-O/Cl bond

lengths. The average Ba-Cl bond length in $BaCl_2$ is 3.1891 Å, while the average Ba-O bond lengths range from 2.6686 Å in Ba-doped calcite to 2.9612 Å in $Ba(NO_3)_2$. In particular, within the explored compositional space, the average Ba-O bond lengths in aragonite and calcite do not significantly change with their Ba concentrations. Our previous studies found that the average bond lengths of Mg-O in carbonates, Ca-O in orthopyroxene, and K-O in feldspars dramatically change with their Mg, Ca, and K concentrations within a certain range (Feng et al., 2014; Wang et al., 2017a, b, 2019; Li et al., 2019), respectively. However, both the average Mg-O and Ca-O bond lengths will not be concentration-dependent when the concentrations are lower than a threshold value. This implies that when Ba/(Ba+Ca) is lower than 1/48, the average Ba-O bond lengths in aragonite and calcite will also not significantly change with Ba concentration. Therefore, the current Ba-doped aragonite and calcite supercells can be used to represent the natural samples with a much lower Ba concentration. The average Ba-O bond length increases in the order of calcite < aragonite < $Ba(H_2PO_4)_2$ ~ $Ba(OH)_2(H_2O)_8$ < witherite ~ $Ba(OH)_2H_2O$ ~ $Ba(OH)_2(H_2O)_3$ < $Ba(PO_3)_2$ < $BaHPO_4$ ~ barite < $Ba_3(PO_4)_2$ < $Ba(NO_3)_2$. The relative order of calcite < aragonite < witherite is consistent with previous theoretical calculations within GGA (Mavromatis et al., 2020). The CN of Ba changes from 6 in calcite to 12 in $Ba(NO_3)_2$. Specially, $Ba_3(PO_4)_2$ and $BaHPO_4$ have two types of Ba atoms, with a ratio of 1:2 between twelve-fold and ten-fold coordinated Ba in $Ba_3(PO_4)_2$ and a ratio of 2:1 between nine-fold and ten-fold coordinated Ba in $BaHPO_4$ (Table 1). As a result, the average CNs of Ba in $Ba_3(PO_4)_2$ and $BaHPO_4$ are 10.7 and 9.7, respectively, rather than integers in other minerals.

In order to obtain the structural properties of aqueous Ba^{2+}, we calculated the partial radial distribution function (PRDF) (Liu et al., 2018) between Ba and O, which can be expressed as:

$$g_{Ba-O}(r) = \frac{N}{\rho N_{Ba} N_O} \langle \sum_{i=1}^{N_{Ba}} \sum_{j=1}^{N_O} \delta(\vec{r} - \vec{R}_i^{Ba} + \vec{R}_j^{O}) \rangle \quad (8)$$

where ρ is the atomic number density and N is the total number of atoms. N_{Ba} and N_O refer to the number of Ba and O atoms, respectively. $\vec{R}$ represents the atomic

coordinates. Our results show that the PRDF of Ba-O pair in $BaCl_2(H_2O)_{70}$ solution mainly distributes in 2.5-3.4 Å with a sharp peak at ~ 2.8 Å and the CN of Ba is ~8 if the cutoff for Ba-O distances is 3.3-3.5 Å (Fig. 1a). The predicted structural properties of aqueous Ba^{2+} in this work agree well with previous experimental measurements (Persson et al., 1995), suggesting the validity of the FPMD simulation. Our previous work found that the structure of aqueous Mg^{2+} will not be significantly affected by the number of water molecules in aqueous models when it is more than 50. As such, we did not test the effect of the number of water molecules (or Ba concentration) on the PRDF of Ba-O pair and the CN as the FPMD simulation on an aqueous model with > $70H_2O$ requires huge computation. Although the Ba concentration in the aqueous model is higher than that in natural seawater, it can be inferred from the simulations of aqueous Mg^{2+} that the PRDF of Ba-O pair and the CN will not significantly change with Ba concentration when Ba:H_2O is lower than 1/70.

3.3 Reduced partition function ratios of $^{137}Ba/^{134}Ba$

The calculated temperature dependences of $10^3\ln\beta$ of all solid phases are shown in Fig. 2a and their polynomial fitting parameters are reported in Table 2. Our results show that $10^3\ln\beta$ ranges from 0.46‰ in $BaCl_2$ to 1.09‰ in aragonite at 300 K. It decreases in the sequence of aragonite > calcite > $Ba(OH)_2H_2O$ > $Ba(OH)_2(H_2O)_8$ ~ witherite > $Ba_3(PO_4)_2$ > $Ba(OH)_2(H_2O)_3$ > $Ba(H_2PO_4)_2$ > $Ba(PO_3)_2$ > $Ba(NO_3)_2$ ~ $BaHPO_4$ > barite > $BaCl_2$. Similar to the average Ba-O bond length, the $10^3\ln\beta$ of aragonite and calcite are insensitive to their Ba concentrations within the explored compositional space (Table 2), suggesting that the Ba concentrations investigated in this study should be lower than the threshold concentration, below which the $10^3\ln\beta$ could be concentration-independent (Feng et al., 2014; Wang et al., 2017a, b, 2019; Li et al., 2019a). As a consequence, the $10^3\ln\beta$ of aragonite and calcite with Ba/(Ba+Ca) of 1/48 should be identical to those with a lower Ba concentration, respectively. The relative order of aragonite > calcite > $Ba(OH)_2(H_2O)_8$ ~ witherite is also supported by previous theoretical results from GGA calculations (Mavromatis et al., 2020). Specially,

the relative $10^3\ln\beta$ differences ($10^3\ln\alpha$) between any two of these four phases predicted in that work are consistent with our results, although both the computational software and pseudopotentials used in this study and Mavromatis et al. (2020) are different (VASP vs. Quantum Espresso). For instance, both two studies show that the $10^3\ln\alpha$ between witherite and $Ba(OH)_2(H_2O)_8$ and between calcite and witherite are 0‰ and 0.16‰ at 300 K, respectively (Fig. 2a and Table 2, Mavromatis et al., 2020). Our previous studies also found that the DFT calculations using different methods within different computational software give similar $10^3\ln\alpha$ values of $^{26}Mg/^{24}Mg$ between dolomite and calcite (Wang et al., 2017a, 2019).

$BaCl_2$ has the smallest $10^3\ln\beta$ among all solid phases, mainly because it has much longer Ba-Cl bonds than Ba-O bonds in other minerals. Generally, the $10^3\ln\beta$ is negatively correlated to the average Ba-O/Cl bond length and minerals with shorter bond lengths are more enriched in heavy Ba isotopes than those with longer bonds (Fig. 3a). As discussed by previous studies (Bigeleisen and Mayer, 1947; Urey, 1947), the relative differences in $10^3\ln\beta$ between minerals are dominantly controlled by their relative bond strengths. Shorter chemical bonds correspond to stronger bond strengths and have higher vibrational frequencies, and thus, are enriched in heavier isotopes relative to longer chemical bonds (Young et al., 2009; Schauble, 2011; Huang et al., 2013, 2014, 2019; Li et al., 2019b). However, some outliers deviate from this tendency (Fig. 3a), suggesting that other factors such as the CN can also significantly affect the bond strength and the $10^3\ln\beta$ (Table 1). For instance, calcite has a shorter average Ba-O bond length than aragonite, but aragonite is enriched in heavy Ba isotopes relative to calcite. This is because Ba is nine-fold coordinated in aragonite but six-fold coordinated in calcite (Table 1). In our previous studies (Feng et al., 2014; Wang et al., 2017a, b, 2019; Li et al., 2019a) on the isotope fractionation of Mg in carbonates, Ca in pyroxenes, and K in feldspars, we found that the $10^3\ln\beta$ are well correlated with their corresponding average Mg-O, Ca-O, and K-O bond lengths, respectively. The bond strengths in these systems are mainly determined by their average bond lengths because other factors such

as the CNs and the bonded anions are the same.

The bond strength can be measured by the force constant (Ducher et al., 2018; Wang et al., 2019; Li et al., 2019b; Mavromatis et al., 2020), as revealed by the linear relationship between the $10^3 \ln\beta$ and the force constant <F> of Ba (Fig. 3b). The variation of $10^3 \ln\beta$ is dominantly controlled by the change of <F> in all minerals. This is consistent with the theoretical analysis (Eq. (4-7)) that $10^3 \ln\beta$ is directly proportional to <F> when the higher-order terms of the Taylor expansions of the expression for β factor are ignored. We also compared the $10^3 \ln\beta$ calculated from full vibrational frequencies using Eq. (1) with the one obtained from <F> using Eq. (7) at 300 K, as shown in Fig. 4. The slope between two sets of $10^3 \ln\beta$ from <F> and full vibrational frequencies is 1.04, suggesting the relative difference between these two methods is about 4% (Fig. 5). For example, the $10^3 \ln\beta$ of witherite from <F> is 0.72‰ at 300 K, which is only 0.02‰ larger than that obtained from full frequencies (Table 1 and 2). Such a difference is only comparable to the uncertainty of $10^3 \ln\beta$ (section 3.1), presumably because the vibrational frequencies related to Ba atom in minerals meet the criteria $\omega_i \leq 1.39$ T =417 cm^{-1}. Thus, it is reliable to calculate $10^3 \ln\beta$ of $^{137}Ba/^{134}Ba$ from <F> using the single-atom approximation.

3.4 Estimating β factor of aqueous Ba^{2+} from force constant

We extracted 121 snapshots from the FPMD trajectory every 250 steps after equilibration and only optimized the atomic positions of Ba. This single-atom relaxation makes the Ba atom in each snapshot stay at the local equilibrium positions but does not change the positions of other atoms around the Ba atom. Then we calculated the force constant matrix of Ba atom using the small displacement method based on the harmonic approximation, as shown in Fig. 1b. Although <F> of Ba in each snapshot is scattered in the time domain, the cumulative average gradually becomes a constant (90.5±0.1 N/m). Because we sampled 121 snapshots from the FPMD trajectory, the statistical error of <F> is negligible. The $10^3 \ln\beta$ of aqueous Ba^{2+} is 0.72‰ at 300 K, similar to those of $Ba(OH)_2(H_2O)_8$, $Ba(OH)_2H_2O$, and witherite (Table 1 and 2).

Relative to aqueous Ba^{2+}, aragonite and calcite are enriched in heavy Ba isotopes, while $Ba(H_2PO_4)_2$, $Ba(PO_3)_2$, $Ba(NO_3)_2$, $BaHPO_4$, barite, and $BaCl_2$ are depleted in heavy Ba isotopes (Fig. 2b). The $10^3\ln\alpha$ between other minerals ($Ba(OH)_2H_2O$, $Ba(OH)_2(H_2O)_8$, witherite, $Ba_3(PO_4)_2$, and $Ba(OH)_2(H_2O)_3$) and aqueous Ba^{2+} is negligible, which is < 0.05‰ at 300 K.

The method used in this study is different from the one used to estimate the β factor of aqueous Mg^{2+} in our previous work (Wang et al., 2019). In that work, we extracted 35 snapshots from the FPMD trajectories every 1000 steps and calculated their full vibrational frequency calculations after atomic relaxation to estimate the final $10^3\ln\beta$. Because not all of the vibrational frequencies related to Mg atom meet the criteria ω_i (cm^{-1}) ≤ 1.39 T at low temperature, the β factor of aqueous Mg^{2+} cannot be simply calculated from <F> using Eq. (7), which would result in a large uncertainty. On the other hand, the use of Eq. (7), if reliable and valid, will greatly reduce the computation cost without the need for full phonon calculations. If the β factors of 121 snapshots for aqueous Ba^{2+} were calculated from full vibrational frequencies using Eq. (1), the total amount of computation would increase by at least two orders of magnitude, which cannot be affordable now.

4. Discussion

4.1 Can aqueous ions be modeled by hydroxide polyhydrates for estimating β factors?

The atoms in solids are bound tightly to each other which makes it resistant to change, whereas those in liquids are free to move around to maintain dynamic positions. As such, estimating the β factors of aqueous ions such as Ba^{2+}, Mg^{2+}, and Zn^{2+} is more complicated and requires higher computational costs than calculating mineral β factors (Kowalski et al., 2013; Ducher et al., 2018; Wang et al., 2019). In order to simplify the theoretical calculations, some previous studies used the crystal structures of hydroxide polyhydrates to model the structures of aqueous ions (Schauble, 2011; Li et al., 2019b;

Mavromatis et al., 2020). For instance, Mavromatis et al. (2020) took the crystal structure of barium hydroxide octahydrate ($Ba(OH)_2(H_2O)_8$) to approach the structure of aqueous Ba^{2+} and Schauble (2011) averaged the $10^3\ln\beta$ of five $Mg(H_2O)_6^{2+}$-bearing crystals to model the β factor of aqueous Mg^{2+}. Our results show that aqueous Ba^{2+} has similar Ba-O bond lengths, CN, force constant, and β factor to those of $Ba(OH)_2(H_2O)_8$, as well as the other two hydroxide polyhydrates, $Ba(OH)_2H_2O$ and $Ba(OH)_2(H_2O)_3$. Thus, it is reliable to estimate the equilibrium Ba isotope fractionation between minerals and aqueous Ba^{2+} using the $10^3\ln\beta$ of $Ba(OH)_2(H_2O)_8$ to represent that of aqueous Ba^{2+}. However, such an interpretation cannot be simply extended to other systems. The equilibrium Mg isotope fractionation between minerals and aqueous Mg^{2+} in Schauble (2011) obviously deviates from the FPMD results (Wang et al., 2019) when five $Mg(H_2O)_6^{2+}$-bearing crystals are taken as analogs to aqueous Mg^{2+}, although these crystals have similar structural properties to aqueous Mg^{2+}. Also, brucite and lizardite have similar average Mg-O bond lengths and the CNs to those of aqueous Mg^{2+}, but they have much larger $10^3\ln\beta$ values than aqueous Mg^{2+} (Wang et al., 2019). These comparisons demonstrate that approaching aqueous ions with hydroxide polyhydrates for estimating β factors, which coincidently works for aqueous Ba^{2+}, should be treated with great caution. We recommend the use of FPMD simulations to obtain the structures of aqueous ions and estimate their β factors from extracted snapshots.

4.2 Equilibrium Ba isotope fractionation between minerals and aqueous Ba^{2+}

4.2.1 Aragonite vs. aqueous Ba^{2+}

Our results show that the equilibrium Ba isotope fractionation factor between aragonite and aqueous Ba^{2+} ($10^3\ln\alpha_{aragonite\text{-}Ba\_aq}$) is 0.36 ± 0.04‰ at 300 K (Table 2 and Fig. 5), suggesting that aragonite will be enriched in heavy Ba isotopes if in thermodynamic equilibrium with aqueous solution. Recently, Mavromatis et al. (2020) performed inorganic precipitation experiments to calibrate the Ba isotope fractionation between calcite/aragonite and aqueous solution ($\Delta^{137/134}Ba_{calcite/aragonite\text{-}solution}$). They found that $\Delta^{137/134}Ba_{aragonite\text{-}solution}$ systematically decreases as a function of increasing

aragonite growth rate. By using a simplified model of Transition State Theory (TST, see the method part in Mavromatis et al., 2020) to fit the relationship between $\Delta^{137/134}Ba_{aragonite\text{-}solution}$ and growth rate, they suggested that the final equilibrium value for $\Delta^{137/134}Ba_{aragonite\text{-}solution}$ is +0.27‰ at 298 K. This experimental value is consistent with our predictions when the analytical error of Ba isotope composition (~0.06‰) and the uncertainty of model fitting (~0.2‰) are considered. The reason for the enrichment of heavy isotopes in aragonite relative to aqueous solution is that compared to aqueous Ba^{2+}, aragonite has much shorter Ba-O bond lengths and a larger CN (~2.8 Å vs. 2.740 Å, ~8 vs. 9), which jointly result in much stronger Ba-O bonds in aragonite (Table 1).

4.2.2 Calcite vs. aqueous Ba^{2+}

The equilibrium Ba isotope fractionation between calcite and aqueous Ba^{2+} ($10^3\ln\alpha_{calcite\text{-}Ba\_aq}$) is 0.14 ± 0.03‰ at 300 K (Table 2 and Fig. 5), suggesting that calcite should be slightly enriched in heavy Ba isotopes relative to aqueous solution at equilibrium. The extend of such fractionation exceeds the analytical uncertainty of Ba isotope composition (~0.06‰) and could be observed in experiments at equilibrium. However, the precipitation experiments conducted by Mavromatis et al. (2020) show that $\Delta^{137/134}Ba_{calcite\text{-}solution}$ does not exhibit a significant variation with calcite growth rate, and the equilibrium value for $\Delta^{137/134}Ba_{calcite\text{-}solution}$ is +0.02‰ at 298 K based on the TST model. Such a near-zero value indicates that no significant Ba isotope fractionation occurs between calcite and aqueous solution, inconsistent with our predictions. This discrepancy, as suggested by Mavromatis et al. (2020), may originate from the Ba incorporation mechanism into the growing calcite crystal. They argued that when a calcite surface CO_3 group substitutes for a water molecule of the first hydration shell of aqueous Ba^{2+} during the sorption process, the structural properties of Ba such as coordination do not undergo significant changes compared to those of aqueous Ba^{2+} (Pokrovsky et al., 2000), and consequently, no Ba isotope fractionation occurs during this process. The second process in which the surface complex transforms to Ba in calcite by substituting for Ca undergoes without further exchange with Ba in solution,

and finally, no significant Ba isotope fractionation occurs between precipitated calcite and solution. Alternatively, when combined with the uncertainty of model fitting (~0.2‰), the observed $\Delta^{137/134}Ba_{calcite\text{-}solution}$ of 0.02 ± 0.2‰ at 298 K is consistent with our results. The small $10^3 ln\alpha_{calcite\text{-}Ba\_aq}$ predicted in this study cannot be well distinguished within the current experimental uncertainty and more well-designed experiments are needed to check this prediction.

4.2.3 Witherite vs. aqueous Ba^{2+}

In contrast to aragonite and calcite, our calculations show that no significant Ba isotope fractionation between witherite and aqueous Ba^{2+} at equilibrium, with the $10^3 ln\alpha_{witherite\text{-}Ba\_aq}$ of -0.02 ± 0.03‰ at 300 K (Table 2 and Fig. 5). This is consistent with small structural differences between witherite and aqueous Ba^{2+}. Compared to eight-fold coordinated Ba in aqueous solution, witherite has a slightly longer average Ba-O bond length than aqueous Ba^{2+} and its Ba atoms are nine-fold coordinated (Table 1). Mavromatis et al. (2016) found that no significant Ba isotope fractionation occurs between witherite and aqueous solution during the witherite dissolution experiments lasting 12500 minutes. These long-term experiments likely have approached isotopic and chemical equilibrium. Meanwhile, they also found that the Ba isotope fractionation between witherite and aqueous solution ($\Delta^{137/134}Ba_{witherite\text{-}solution}$) is -0.07 ± 0.04‰ at 298 K during witherite precipitation caused by a pH increase. These experimental observations are consistent with our calculated results within the uncertainty (Fig. 5). However, the other two experimental studies (von Allmen et al., 2010; Böttcher et al., 2018) observed $\Delta^{137/134}Ba_{witherite\text{-}solution}$ ranging from -0.32‰ to -0.06‰ at 294-333 K during witherite precipitation from supersaturated solutions, which significantly deviates from the results of this study and Mavromatis et al. (2016). This difference likely results from kinetic effects stemmed from precipitation conditions such as the precipitation rate of witherite (Mavromatis et al., 2016; Böttcher et al., 2018). In particular, Mavromatis et al. (2016) suggested that the exchange of Ba continuously occurs between witherite and solution after the achievement of chemical equilibrium,

which involves several layers below the witherite surface. This indicates that the time required for the achievement of isotopic exchange equilibrium is longer than that observed for chemical equilibrium. As a consequence, more time and effort are needed to achieve and confirm isotopic equilibrium between phases in room-temperature experiments for determining the equilibrium isotope fractionation (Wimpenny et al., 2014).

4.2.4 Barite vs. aqueous Ba^{2+}

The $10^3 \ln\alpha_{barite\text{-}Ba\_aq}$ is -0.17 ± 0.03‰ at 300 K (Table 2 and Fig. 5), suggesting the enrichment of heavy Ba isotopes in aqueous solution relative to barite at equilibrium. This is because the average Ba-O bond length in barite is significantly longer than that of aqueous Ba^{2+} (Table 1), although barite has a larger Ba CN than aqueous Ba^{2+}. Two previous experimental studies (von Allmen et al., 2010; Böttcher et al., 2018) have investigated the Ba isotope fractionation between barite and aqueous solution ($\Delta^{137/134}Ba_{barite\text{-}solution}$) and observed a range of -0.27‰ - -0.21‰ for $\Delta^{137/134}Ba_{barite\text{-}solution}$ at 294 K during barite precipitation, consistent with our results within the experimental uncertainty (~0.07‰). However, one concern with such experiments is that achieving Ba isotopic exchange equilibrium between two phases at low temperatures has not been confirmed. Thus, it is unknown to what extent chemical kinetic effects control the finally observed isotopic fractionation. More experimental researches are needed to investigate how kinetic factors affect the $\Delta^{137/134}Ba_{barite\text{-}solution}$ and further determine the equilibrium value.

4.3 Implications for Ba isotope geochemistry

Previous studies have widely investigated the Ba concentration and Ba isotope composition in the modern oceans (Horner et al., 2015; Bates et al., 2017; Hsieh and Henderson, 2017; Bridgestock et al., 2018). They found that $\delta^{137/134}Ba$ ($\delta^{137/134}Ba=0.75*\delta^{138/134}Ba$) values decrease from ~ +0.50‰ to +0.15‰ from the surface to the deep ocean, while dissolved Ba concentrations increase from ~ 40 to 100 nmol kg^{-1}. There is a strong negative correlation between $\delta^{137/134}Ba$ and Ba

concentration (Bridgestock et al., 2018). Three main processes were proposed to explain these observations (Horner et al., 2015; Bates et al., 2017; Hsieh and Henderson, 2017; Bridgestock et al., 2018): (1) the Ba removal such as the barite precipitation; (2) Ba regeneration from the subsequent dissolution of barite particles in the under-saturated water column; (3) ocean circulation and mixing between different water masses. A steady-state fractionation model was previously used to describe the effect of Ba removal on the $\delta^{137/134}$Ba profile (Horner et al., 2015; Bates et al., 2017; Hsieh and Henderson, 2017; Bridgestock et al., 2018), which can be expressed as:

$$\delta^{137/134}Ba_{diss} = \delta^{137/134}Ba_{diss,0} + 1000 \times (\alpha_{diss/part} - 1) \times (1-f_{diss}) \quad (9)$$

where $\delta^{137/134}Ba_{diss}$ and $\delta^{137/134}Ba_{diss,0}$ are the current and the initial Ba compositions, respectively. $\alpha_{diss/part}$ is the fractionation factor of $^{137}Ba/^{134}Ba$ between dissolved and particulate phases and f_{diss} is the fraction of dissolved Ba remaining in seawater relative to the initial concentration.

Fitting models to linear regressions of $\delta^{137/134}Ba_{diss}$ and the dissolved Ba concentration based on different initial concentrations and $\delta^{137/134}Ba_{diss,0}$ demonstrate that the $\alpha_{diss/part}$ ranges from 1.00023 to 1.00041, corresponding to the $\Delta^{137/134}Ba_{diss-part}$ of +0.23-+0.41‰ (Bridgestock et al., 2018). Such a fractionation value exceeds the estimate from this study (+0.17‰ at 300 K), indicating that the Ba removal resulted from inorganic barite precipitation at equilibrium cannot account for the observed variation of 0.35‰ in $\delta^{137/134}Ba_{diss}$. The Ba addition from precipitated barite particles to deep under-saturated waters by regeneration processes can also somewhat explain the profiles of Ba concentration and $\delta^{137/134}Ba_{diss}$, but it also requires that the $\delta^{137/134}$Ba difference between solution and barite is +0.4-0.6‰ (Bridgestock et al., 2018). The precipitation of inorganic barite was thought to unlikely occur in the upper water column because it is slightly undersaturated with respect to barite (Monnin and Cividini, 2006). Instead, the pelagic barite precipitation was suggested to occur in particle-associated microenvironments where additional barium and sulfate ions are supplied by heterotrophic remineralization of organic matter to achieve barite saturation, and the

observed $\Delta^{137/134}Ba_{diss\text{-}barite}$ is up to +0.32‰ (Horner et al., 2017), within the expected range (+0.23-+0.41‰). This indicates that some kinetic factors, such as the mineral growth rate and the chemical diffusion, likely controls the Ba isotope fractionation during the formation of natural barite. For instance, previous experimental studies observed increasing enrichment of the solid in light isotopes with precipitation rate for Mg in magnesite (Pearce et al., 2012), Ca in calcite (Tang et al., 2012), Sr in strontianite (Mavromatis et al., 2017), and Ba in aragonite (Mavromatis et al., 2020).

In addition, given that the external riverine and hydrothermal inputs could somewhat affect the Ba concentrations and $\delta^{137/134}Ba$ values of surface and deep waters respectively (Cao et al., 2016; Nielsen et al., 2018; Gou et al., 2020; Li et al., 2020), bimodal mixing models between waters with different Ba concentrations and $\delta^{137/134}Ba$ values can also reproduce the observed correlation between $\delta^{137/134}Ba$ and Ba concentration (Bridgestock et al., 2018). The ambiguity of interpretation on controlling factors of seawater $\delta^{137/134}Ba$, however, may impede the use of Ba isotope composition of sedimentary authigenic Ba, which is concentrated in barite (Bridgestock et al., 2018), as a proxy for past ocean Ba cycling and changes in export production. Overall, the observed profiles of Ba concentration and $\delta^{137/134}Ba$ in the modern oceans are likely induced by the Ba removal effect of biogenic barite and/or the water mixing between different reservoirs.

It was suggested that Ba isotopes in aragonitic corals may be used as a tracer to construct the past $\delta^{137/134}Ba$ of seawater. Previous studies found that the Ba isotope fractionation between coral and seawater ranges from -0.3‰ to -0.15‰ (Pretet et al., 2015; Hemsing et al., 2018; Liu et al., 2019), inconsistent with the direction of equilibrium fractionation between aragonite and aqueous solution predicted in this study. The probable precipitation of witherite in the coralline aragonite skeletons was proposed to explain the variation of Ba/Ca ratios in the corals (Liu et al., 2019). Because no significant fractionation occurs between witherite and solution at equilibrium (Fig. 5), the equilibrium processes cannot explain the observed negative fractionation, and

kinetic effects should play an important role in the Ba isotope partition between natural aragonite and seawater. Mavromatis et al. (2020) found that $\Delta^{137/134}Ba_{aragonite\text{-}solution}$ decreases as a function of increasing precipitation rate during inorganic precipitation experiments, and therefore, the negative Ba isotope fractionation between coral and seawater could be caused by the relatively fast growth of aragonite. Light isotopes were also found to be increasingly enriched in carbonates with the precipitation rate in other systems such as Mg in magnesite (Pearce et al., 2012) and Ca in calcite (Tang et al., 2012). Beyond that, the presence of Mg organic complexes could show a significant impact on the Mg isotope composition of precipitated Mg-bearing minerals. Thus, some environmental factors such as Ba speciation in the fluid where aragonite precipitates are also important for understanding the Ba isotope fractionation. In addition, the vital effects in corals could be one of the major sources for the kinetic fractionation (Pretet et al., 2015), but the nature of vital effects is still poorly understood. Further systematic studies are needed to investigate the controlling factors on Ba isotope fractionation during the formation of aragonitic corals.

5. Conclusions

Equilibrium Ba isotope fractionation factors between minerals and aqueous solution were calculated based on the DFT. The average Ba-Cl bond length in $BaCl_2$ is 3.1891 Å, while the average Ba-O bond lengths range from 2.6686 Å in Ba-doped calcite to 2.9612 Å in $Ba(NO_3)_2$. The CN of Ba changes from 6 in calcite to 12 in $Ba(NO_3)_2$. For aqueous Ba^{2+}, we conducted the FPMD simulation to obtain its structural properties. The PRDF of Ba-O pair in $BaCl_2(H_2O)_{70}$ solution has a sharp peak at ~ 2.8 Å and the CN of Ba is ~8, consistent with previous experimental measurements (Persson et al., 1995). We extracted 121 snapshots from the FPMD trajectory to estimate the β-factor of aqueous Ba^{2+} from the force constant. For minerals, the β-factors were calculated from vibrational frequencies based on the DFT with the periodic boundary conditions.

The β-factor decreases in the sequence of aragonite > calcite > $Ba(OH)_2H_2O$ > aqueous Ba^{2+} ~ $Ba(OH)_2(H_2O)_8$ ~ witherite > $Ba_3(PO_4)_2$ > $Ba(OH)_2(H_2O)_3$ > $Ba(H_2PO_4)_2$ > $Ba(PO_3)_2$ > $Ba(NO_3)_2$ ~ $BaHPO_4$ > barite > $BaCl_2$. Generally, the $10^3\ln\beta$ is negatively correlated to the average Ba-O/Cl bond length, but the CN also affects the bond strength and the $10^3\ln\beta$. The $10^3\ln\beta$ is directly proportional to the force constant <F>, suggesting that the bond strength can be measured by the force constant. Our results show that compared to aqueous Ba^{2+}, aragonite and calcite are enriched in heavy Ba isotopes, while barite is depleted in heavy Ba isotopes. No significant Ba isotope fractionation occurs between witherite and aqueous Ba^{2+}. The $10^3\ln\alpha_{aragonite\text{-}Ba\_aq}$ and $10^3\ln\alpha_{witherite\text{-}Ba\_aq}$ are 0.36‰ and -0.02‰ at 300 K, respectively, consistent with experimental results at equilibrium. The $10^3\ln\alpha_{barite\text{-}Ba\_aq}$ is only -0.17‰ at 300 K, indicating that the Ba removal resulted from inorganic barite precipitation cannot account for a variation of 0.35‰ in seawater $\delta^{137/134}Ba$. In addition, the depletion of heavy Ba isotopes observed in corals relative to seawater suggests that kinetic effects play an important role in coral growth. This study provides reliable data for the equilibrium Ba isotope fractionation between minerals and aqueous Ba^{2+}, which is of great importance for the applications of Ba isotopes in low-temperature geochemistry.

Acknowledgments

This study is financially supported by the Strategic Priority Research Program (B) of the Chinese Academy of Sciences (XDB18000000) and the Natural Science Foundation of China (41925017, 41721002, 41325011). The computations were conducted in the Supercomputing Center of the University of Science and Technology of China. We are grateful to the constructive comments from three anonymous reviewers and editorial handling by Marc Blanchard.

References

Alibert C. and Kinsley L. (2008) A 170-year Sr/Ca and Ba/Ca coral record from the western Pacific warm pool: 1. What can we learn from an unusual coral record? *J. Geophys. Res. Ocean.* **113**, 1–13.

von Allmen K., Böttcher M. E., Samankassou E. and Nägler T. F. (2010) Barium isotope fractionation in the global barium cycle: First evidence from barium minerals and precipitation experiments. *Chem. Geol.* **277**, 70–77. Available at: http://dx.doi.org/10.1016/j.chemgeo.2010.07.011.

Angeli I. (2004) A consistent set of nuclear rms charge radii: properties of the radius surface R(N,Z). *At. Data Nucl. Data Tables* **87**, 185–206. Available at: https://linkinghub.elsevier.com/retrieve/pii/S0092640X04000166.

Antao S. M. and Hassan I. (2007) BaCO3: high-temperature crystal structures and the Pmcn→R3m phase transition at 811°C. *Phys. Chem. Miner.* **34**, 573–580. Available at: http://link.springer.com/10.1007/s00269-007-0172-8.

Bates S. L., Hendry K. R., Pryer H. V., Kinsley C. W., Pyle K. M., Woodward E. M. S. and Horner T. J. (2017) Barium isotopes reveal role of ocean circulation on barium cycling in the Atlantic. *Geochim. Cosmochim. Acta* **204**, 286–299. Available at: http://dx.doi.org/10.1016/j.gca.2017.01.043.

BenChaabane T., Smiri L. and Bulou A. (2004) Vibrational study and crystal structure refinement of BaHPO4. *Solid State Sci.* **6**, 197–204. Available at: https://linkinghub.elsevier.com/retrieve/pii/S1293255803002577.

Bigeleisen J. and Mayer M. G. (1947) Calculation of Equilibrium Constants for Isotopic Exchange Reactions. *J. Chem. Phys.* **15**, 261. Available at: http://scitation.aip.org/content/aip/journal/jcp/15/5/10.1063/1.1746492.

Blöchl P. E. (1994) Projector augmented-wave method. *Phys. Rev. B* **50**, 17953–17979. Available at: http://link.aps.org/doi/10.1103/PhysRevB.50.17953.

Böttcher M. E., Neubert N., von Allmen K., Samankassou E. and Nägler T. F. (2018) Barium isotope fractionation during the experimental transformation of aragonite to witherite and of gypsum to barite, and the effect of ion (de)solvation. *Isotopes Environ. Health Stud.* **54**, 324–335. Available at: https://www.tandfonline.com/doi/full/10.1080/10256016.2018.1430692.

Bridgestock L., Hsieh Y. Te, Porcelli D., Homoky W. B., Bryan A. and Henderson G. M. (2018) Controls on the barium isotope compositions of marine sediments. *Earth Planet. Sci. Lett.* **481**, 101–110. Available at: https://doi.org/10.1016/j.epsl.2017.10.019.

Cao Z., Siebert C., Hathorne E. C., Dai M. and Frank M. (2016) Constraining the oceanic barium cycle with stable barium isotopes. *Earth Planet. Sci. Lett.* **434**, 1–9. Available at: http://dx.doi.org/10.1016/j.epsl.2015.11.017.

Carter L. B., Skora S., Blundy J. D., De Hoog J. C. M. and Elliott T. (2015) An Experimental Study of Trace Element Fluxes from Subducted Oceanic Crust. *J. Petrol.* **56**, 1585–1606. Available at: https://academic.oup.com/petrology/article-lookup/doi/10.1093/petrology/egv046.

Ducher M., Blanchard M. and Balan E. (2018) Equilibrium isotopic fractionation between aqueous Zn and minerals from first-principles calculations. *Chem. Geol.*, 1–9. Available at: http://dx.doi.org/10.1016/j.chemgeo.2018.02.040.

Eagle M., Paytan A., Arrigo K. R., van Dijken G. and Murray R. W. (2003) A comparison between excess barium and barite as indicators of carbon export. *Paleoceanography* **18**, n/a-n/a.

Elliott T., Plank T., Zindler A., White W. and Bourdon B. (1997) Element transport from slab to volcanic front at the Mariana arc. *J. Geophys. Res. Solid Earth* **102**, 14991–15019. Available at: http://doi.wiley.com/10.1029/97JB00788.

Feng C., Qin T., Huang S., Wu Z. and Huang F. (2014) First-principles investigations of equilibrium calcium isotope fractionation between clinopyroxene and Ca-doped orthopyroxene. *Geochim. Cosmochim. Acta* **143**, 132–142. Available at: http://dx.doi.org/10.1016/j.gca.2014.06.002.

Gonneea M. E. and Paytan A. (2006) Phase associations of barium in marine sediments. *Mar. Chem.* **100**, 124–135. Available at: https://linkinghub.elsevier.com/retrieve/pii/S0304420305002409.

Gou L.-F., Jin Z., Galy A., Gong Y.-Z., Nan X.-Y., Jin C., Wang X.-D., Bouchez J., Cai H.-M., Chen J.-B., Yu H.-M. and Huang F. (2020) Seasonal riverine barium isotopic variation in the middle Yellow River: Sources and fractionation. *Earth Planet. Sci. Lett.* **531**, 115990. Available at: https://doi.org/10.1016/j.epsl.2019.115990.

Grenier J.-C., Martin C., Durif-Varambon A., Tranqui D. and Guitel J.-C. (1967) Une nouvelle forme du métaphosphate de baryum Ba(PO3)2. *Bull. la Société française Minéralogie Cristallogr.* **90**, 24–31. Available at: https://www.persee.fr/doc/bulmi_0037-9328_1967_num_90_1_6062.

Hemsing F., Hsieh Y.-T., Bridgestock L., Spooner P. T., Robinson L. F., Frank N. and Henderson G. M. (2018) Barium isotopes in cold-water corals. *Earth Planet. Sci. Lett.* **491**, 183–192. Available at: https://doi.org/10.1016/j.epsl.2018.03.040.

Horner T. J., Kinsley C. W. and Nielsen S. G. (2015) Barium-isotopic fractionation in seawater mediated by barite cycling and oceanic circulation. *Earth Planet. Sci. Lett.* **430**, 511–522. Available at: http://dx.doi.org/10.1016/j.epsl.2015.07.027.

Horner T. J., Pryer H. V., Nielsen S. G., Crockford P. W., Gauglitz J. M., Wing B. A. and Ricketts R. D. (2017) Pelagic barite precipitation at micromolar ambient sulfate. *Nat. Commun.* **8**, 1342. Available at: http://www.nature.com/articles/s41467-017-01229-5.

Hsieh Y.-T. and Henderson G. M. (2017) Barium stable isotopes in the global ocean: Tracer of Ba inputs and utilization. *Earth Planet. Sci. Lett.* **473**, 269–278. Available at: http://dx.doi.org/10.1016/j.epsl.2017.06.024.

Huang F., Chen L., Wu Z. and Wang W. (2013) First-principles calculations of equilibrium Mg isotope fractionations between garnet, clinopyroxene, orthopyroxene, and olivine: Implications for Mg isotope thermometry. *Earth Planet. Sci. Lett.* **367**, 61–70. Available at:

http://dx.doi.org/10.1016/j.epsl.2013.02.025.
Huang F., Wu Z., Huang S. and Wu F. (2014) First-principles calculations of equilibrium silicon isotope fractionation among mantle minerals. *Geochim. Cosmochim. Acta* **140**, 509–520. Available at: http://dx.doi.org/10.1016/j.gca.2014.05.035.
Huang F., Zhou C., Wang W., Kang J. and Wu Z. (2019) First-principles calculations of equilibrium Ca isotope fractionation: Implications for oldhamite formation and evolution of lunar magma ocean. *Earth Planet. Sci. Lett.* **510**, 153–160. Available at: https://doi.org/10.1016/j.epsl.2018.12.034.
Hull S., Norberg S. T., Ahmed I., Eriksson S. G. and Mohn C. E. (2011) High temperature crystal structures and superionic properties of SrCl2, SrBr2, BaCl2 and BaBr2. *J. Solid State Chem.* **184**, 2925–2935. Available at: https://linkinghub.elsevier.com/retrieve/pii/S0022459611004865.
Kerisit S. N. and Prange M. P. (2019) Ab Initio Molecular Dynamics Simulation of Divalent Metal Cation Incorporation in Calcite: Implications for Interpreting X-ray Absorption Spectroscopy Data. *ACS Earth Sp. Chem.* **3**, 2582–2592. Available at: https://pubs.acs.org/doi/10.1021/acsearthspacechem.9b00247.
Kessel R., Schmidt M. W., Ulmer P. and Pettke T. (2005) Trace element signature of subduction-zone fluids, melts and supercritical liquids at 120–180 km depth. *Nature* **437**, 724–727. Available at: http://www.nature.com/articles/nature03971.
Kowalski P. M., Wunder B. and Jahn S. (2013) Ab initio prediction of equilibrium boron isotope fractionation between minerals and aqueous fluids at high P and T. *Geochim. Cosmochim. Acta* **101**, 285–301. Available at: http://dx.doi.org/10.1016/j.gca.2012.10.007.
Kuske P., Engelen B., Henning J., Lutz H. D., Fuess H. and Gregson D. (1988) Neutron diffraction study of Sr(OH)2 · H2O and β-Ba(OH)2 · H20. *Zeitschrift für Krist. - Cryst. Mater.* **183**. Available at: http://www.degruyter.com/view/j/zkri.1988.183.issue-1-4/zkri.1988.183.14.319/zkri.1988.183.14.319.xml.
LaVigne M., Grottoli A. G., Palardy J. E. and Sherrell R. M. (2016) Multi-colony calibrations of coral Ba/Ca with a contemporaneous in situ seawater barium record. *Geochim. Cosmochim. Acta* **179**, 203–216.
Lea D. W., Shen G. T. and Boyle E. A. (1989) Coralline barium records temporal variability in equatorial Pacific upwelling. *Nature* **340**, 373–376. Available at: http://www.nature.com/articles/340373a0.
Lewis S. E., Lough J. M., Cantin N. E., Matson E. G., Kinsley L., Bainbridge Z. T. and Brodie J. E. (2018) A critical evaluation of coral Ba/Ca, Mn/Ca and Y/Ca ratios as indicators of terrestrial input: New data from the Great Barrier Reef, Australia. *Geochim. Cosmochim. Acta* **237**, 131–154. Available at: https://doi.org/10.1016/j.gca.2018.06.017.
Li W.-Y., Yu H.-M., Xu J., Halama R., Bell K., Nan X.-Y. and Huang F. (2020) Barium isotopic composition of the mantle: Constraints from carbonatites.

Geochim. Cosmochim. Acta **278**, 235–243. Available at: https://doi.org/10.1016/j.gca.2019.06.041.

Li Y., Wang W., Huang S., Wang K. and Wu Z. (2019a) First-principles investigation of the concentration effect on equilibrium fractionation of K isotopes in feldspars. *Geochim. Cosmochim. Acta* **245**, 374–384. Available at: https://linkinghub.elsevier.com/retrieve/pii/S0016703718306264.

Li Y., Wang W., Wu Z. and Huang S. (2019b) First-principles investigation of equilibrium K isotope fractionation among K-bearing minerals. *Geochim. Cosmochim. Acta* **264**, 30–42. Available at: https://doi.org/10.1016/j.gca.2019.07.038.

Liu X., Qi Y., Zheng D., Zhou C., He L. and Huang F. (2018) Diffusion coefficients of Mg isotopes in MgSiO 3 and Mg 2 SiO 4 melts calculated by first-principles molecular dynamics simulations. *Geochim. Cosmochim. Acta* **223**, 364–376. Available at: https://doi.org/10.1016/j.gca.2017.12.007.

Liu Y., Li X., Zeng Z., Yu H.-M., Huang F., Felis T. and Shen C.-C. (2019) Annually-resolved coral skeletal δ138/134Ba records: A new proxy for oceanic Ba cycling. *Geochim. Cosmochim. Acta* **247**, 27–39. Available at: https://doi.org/10.1016/j.gca.2018.12.022.

Lutz H. D., Kellersohn T. and Vogt T. (1990) Hydrogen bonding in barium hydroxide trihydrate by neutron diffraction. *Acta Crystallogr. Sect. C Cryst. Struct. Commun.* **46**, 361–363. Available at: http://scripts.iucr.org/cgi-bin/paper?S0108270189006761.

Manoun B., Popović L., De Waal D. and Verryn S. M. C. (2003) Rietveld refinements of a new solid solution Ba (3− x) Sr x (PO 4) 2 (0≤ x ≤3). *Powder Diffr.* **18**, 122–127. Available at: https://www.cambridge.org/core/product/identifier/S0885715600007636/type/journal_article.

Mavromatis V., Harrison A. L., Eisenhauer A. and Dietzel M. (2017) Strontium isotope fractionation during strontianite (SrCO3) dissolution, precipitation and at equilibrium. *Geochim. Cosmochim. Acta* **218**, 201–214. Available at: https://doi.org/10.1016/j.gca.2017.08.039.

Mavromatis V., van Zuilen K., Blanchard M., van Zuilen M., Dietzel M. and Schott J. (2020) Experimental and theoretical modelling of kinetic and equilibrium Ba isotope fractionation during calcite and aragonite precipitation. *Geochim. Cosmochim. Acta* **269**, 566–580. Available at: https://doi.org/10.1016/j.gca.2019.11.007.

Mavromatis V., van Zuilen K., Purgstaller B., Baldermann A., Nägler T. F. and Dietzel M. (2016) Barium isotope fractionation during witherite (BaCO3) dissolution, precipitation and at equilibrium. *Geochim. Cosmochim. Acta* **190**, 72–84. Available at: https://linkinghub.elsevier.com/retrieve/pii/S0016703716303544.

McCulloch M., Fallon S., Wyndham T., Hendy E., Lough J. and Barnes D. (2003)

Coral record of increased sediment flux to the inner Great Barrier Reef since European settlement. *Nature* **421**, 727–730.

Méheut M., Lazzeri M., Balan E. and Mauri F. (2009) Structural control over equilibrium silicon and oxygen isotopic fractionation: A first-principles density-functional theory study. *Chem. Geol.* **258**, 28–37. Available at: http://dx.doi.org/10.1016/j.chemgeo.2008.06.051.

Miynre M., Minero I. and Ssrn-rcur H. M. (1978) Crystal structures and sulphate force constants ofbarite, celestite, and anglesite. *Phys. Chem. Miner.* **63**, 506–510.

Monnin C. and Cividini D. (2006) The saturation state of the world's ocean with respect to (Ba,Sr)SO4 solid solutions. *Geochim. Cosmochim. Acta* **70**, 3290–3298. Available at: https://linkinghub.elsevier.com/retrieve/pii/S0016703706001682.

Montaggioni L. F., Le Cornec F., Corrège T. and Cabioch G. (2006) Coral barium/calcium record of mid-Holocene upwelling activity in New Caledonia, South-West Pacific. *Palaeogeogr. Palaeoclimatol. Palaeoecol.* **237**, 436–455.

Montanari B., Civalleri B., Zicovich-Wilson C. M. and Dovesi R. (2006) Influence of the exchange-correlation functional in all-electron calculations of the vibrational frequencies of corundum (α-Al2O3). *Int. J. Quantum Chem.* **106**, 1703–1714. Available at: http://doi.wiley.com/10.1002/qua.20938.

Moyer R. P., Grottoli A. G. and Olesik J. W. (2012) A multiproxy record of terrestrial inputs to the coastal ocean sing minor and trace elements (Ba/Ca, Mn/Ca, Y/Ca) and carbon isotopes (d13C, Δ14C) in a nearshore coral from Puerto Rico. *Paleoceanography* **27**, 1–14.

Nan X. Y., Yu H. M., Rudnick R. L., Gaschnig R. M., Xu J., Li W. Y., Zhang Q., Jin Z. D., Li X. H. and Huang F. (2018) Barium isotopic composition of the upper continental crust. *Geochim. Cosmochim. Acta* **233**, 33–49. Available at: https://doi.org/10.1016/j.gca.2018.05.004.

Nielsen S. G., Horner T. J., Pryer H. V, Blusztajn J., Shu Y., Kurz M. D. and Le Roux V. (2018) Barium isotope evidence for pervasive sediment recycling in the upper mantle. *Sci. Adv.* **4**, eaas8675. Available at: https://advances.sciencemag.org/lookup/doi/10.1126/sciadv.aas8675.

Nielsen S. G., Shu Y., Auro M., Yogodzinski G., Shinjo R., Plank T., Kay S. M. and Horner T. J. (2020) Barium isotope systematics of subduction zones. *Geochim. Cosmochim. Acta* **275**, 1–18. Available at: https://doi.org/10.1016/j.gca.2020.02.006.

Nowotny H. and Heger G. (1983) Structure refinement of strontium nitrate, Sr(NO3)2, and barium nitrate, Ba(NO3)2. *Acta Crystallogr. Sect. C Cryst. Struct. Commun.* **39**, 952–956. Available at: http://scripts.iucr.org/cgi-bin/paper?S0108270183006976.

Paytan A. and Griffith E. M. (2007) Marine barite: Recorder of variations in ocean export productivity. *Deep. Res. Part II Top. Stud. Oceanogr.* **54**, 687–705.

Pearce C. R., Saldi G. D., Schott J. and Oelkers E. H. (2012) Isotopic fractionation during congruent dissolution, precipitation and at equilibrium: Evidence from Mg isotopes. *Geochim. Cosmochim. Acta* **92**, 170–183. Available at: http://dx.doi.org/10.1016/j.gca.2012.05.045.

Perdew J. P., Burke K. and Ernzerhof M. (1996) Generalized Gradient Approximation Made Simple. *Phys. Rev. Lett.* **77**, 3865–3868. Available at: http://www.ncbi.nlm.nih.gov/pubmed/10062328%5Cnhttp://link.aps.org/doi/10.1103/PhysRevLett.77.3865%5Cnhttp://link.aps.org/abstract/PRL/v77/p3865%5Cnhttp://link.aps.org/doi/10.1103/PhysRevLett.77.3865.

Persson I., Sandström M. and Yokoyama H. (1995) Structure of the Solvated Strontium and Barium Ions in Aqueous, Dimethyl Sulfoxide and Pyridine Solution, and Crystal Structure of Strontium and Barium Hydroxide Octahydrate. *Zeitschrift für Naturforsch. A* **50**, 287. Available at: https://www.degruyter.com/view/j/zna.1995.50.issue-1/zna-1995-0105/zna-1995-0105.xml.

Pokrovsky O. S., Mielczarski J. A., Barres O. and Schott J. (2000) Surface Speciation Models of Calcite and Dolomite/Aqueous Solution Interfaces and Their Spectroscopic Evaluation. *Langmuir* **16**, 2677–2688. Available at: https://pubs.acs.org/doi/10.1021/la980905e.

Prelesnik B., Herak R., Čurić M. and Krstanović I. (1978) The crystal structure of orthorhombic barium dihydrogenphosphate. *Acta Crystallogr. Sect. B* **34**, 76–78. Available at: http://scripts.iucr.org/cgi-bin/paper?S0567740878002320.

Pretet C., van Zuilen K., Nägler T. F., Reynaud S., Böttcher M. E. and Samankassou E. (2015) Constraints on barium isotope fractionation during aragonite precipitation by corals. *Depos. Rec.* **1**, 118–129.

Reeder R. J., Lamble G. M. and Northrup P. A. (1999) XAFS study of the coordination and local relaxation around Co2+, Zn2+, Pb2+, and Ba2+ trace elements in calcite. *Am. Mineral.* **84**, 1049–1060. Available at: https://pubs.geoscienceworld.org/ammin/article/84/7-8/1049-1060/43707.

Richet P., Bottinga Y. and Javoy M. (1977) A Review of Hydrogen, Carbon, Nitrogen, Oxygen, Sulphur, and Chlorine Stable Isotope Fractionation Among Gaseous Molecules. *Annu. Rev. Earth Planet. Sci.* **5**, 65–110. Available at: http://adsabs.harvard.edu/full/1977AREPS...5...65R.

Rudnick R. L. and Gao S. (2014) Composition of the Continental Crust. In *Treatise on Geochemistry* Elsevier. pp. 1–51. Available at: http://dx.doi.org/10.1016/B978-0-08-095975-7.00301-6.

Salters V. J. M. and Stracke A. (2004) Composition of the depleted mantle. *Geochemistry, Geophys. Geosystems* **5**.

Schauble E. A. (2011) First-principles estimates of equilibrium magnesium isotope fractionation in silicate, oxide, carbonate and hexaaquamagnesium(2+) crystals. *Geochim. Cosmochim. Acta* **75**, 844–869. Available at: http://linkinghub.elsevier.com/retrieve/pii/S0016703710006332.

Shen J., Schoepfer S. D., Feng Q., Zhou L., Yu J., Song H., Wei H. and Algeo T. J. (2015) Marine productivity changes during the end-Permian crisis and Early Triassic recovery. *Earth-Science Rev.* **149**, 136–162. Available at: http://dx.doi.org/10.1016/j.earscirev.2014.11.002.

Sun S. -s. and McDonough W. F. (1989) Chemical and isotopic systematics of oceanic basalts: implications for mantle composition and processes. *Geol. Soc. London, Spec. Publ.* **42**, 313–345. Available at: http://sp.lyellcollection.org/lookup/doi/10.1144/GSL.SP.1989.042.01.19.

Tang J., Niedermayr A., Köhler S. J., Böhm F., Kısakürek B., Eisenhauer A. and Dietzel M. (2012) Sr2+/Ca2+ and 44Ca/40Ca fractionation during inorganic calcite formation: III. Impact of salinity/ionic strength. *Geochim. Cosmochim. Acta* **77**, 432–443. Available at: https://linkinghub.elsevier.com/retrieve/pii/S0016703711006387.

Togo A. and Tanaka I. (2015) First principles phonon calculations in materials science. *Scr. Mater.* **108**, 1–5. Available at: http://dx.doi.org/10.1016/j.scriptamat.2015.07.021.

Urey H. C. (1947) The thermodynamic properties of isotopic substances ed. S.-I. Karato. *J. Chem. Soc.*, 562. Available at: http://doi.wiley.com/10.1002/9781118529492.

Wang W., Qin T., Zhou C., Huang S., Wu Z. and Huang F. (2017a) Concentration effect on equilibrium fractionation of Mg-Ca isotopes in carbonate minerals: Insights from first-principles calculations. *Geochim. Cosmochim. Acta* **208**, 185–197. Available at: http://dx.doi.org/10.1016/j.gca.2017.03.023.

Wang W. and Wu Z. (2018) Elasticity of Corundum at High Pressures and Temperatures: Implications for Pyrope Decomposition and Al-Content Effect on Elastic Properties of Bridgmanite. *J. Geophys. Res. Solid Earth* **123**, 1201–1216. Available at: http://doi.wiley.com/10.1002/2017JB015088.

Wang W., Zhou C., Liu Y., Wu Z. and Huang F. (2019) Equilibrium Mg isotope fractionation among aqueous Mg2+, carbonates, brucite and lizardite: Insights from first-principles molecular dynamics simulations. *Geochim. Cosmochim. Acta* **250**, 117–129. Available at: https://doi.org/10.1016/j.gca.2019.01.042.

Wang W., Zhou C., Qin T., Kang J., Huang S., Wu Z. and Huang F. (2017b) Effect of Ca content on equilibrium Ca isotope fractionation between orthopyroxene and clinopyroxene. *Geochim. Cosmochim. Acta* **219**, 44–56. Available at: http://dx.doi.org/10.1016/j.gca.2017.09.022.

Wentzcovitch R. M., Yu Y. G. and Wu Z. (2010) Thermodynamic Properties and Phase Relations in Mantle Minerals Investigated by First Principles Quasiharmonic Theory. *Rev. Mineral. Geochemistry* **71**, 59–98. Available at: http://rimg.geoscienceworld.org.

Wimpenny J., Colla C. A., Yin Q. Z., Rustad J. R. and Casey W. H. (2014) Investigating the behaviour of Mg isotopes during the formation of clay minerals. *Geochim. Cosmochim. Acta* **128**, 178–194. Available at:

http://dx.doi.org/10.1016/j.gca.2013.12.012.

Yang S. and Liu Y. (2015) Nuclear volume effects in equilibrium stable isotope fractionations of mercury, thallium and lead. *Sci. Rep.* **5**, 1–12. Available at: http://dx.doi.org/10.1038/srep12626.

Young E. D., Tonui E., Manning C. E., Schauble E. and Macris C. A. (2009) Spinel–olivine magnesium isotope thermometry in the mantle and implications for the Mg isotopic composition of Earth. *Earth Planet. Sci. Lett.* **288**, 524–533. Available at: http://dx.doi.org/10.1016/j.epsl.2009.10.014.

Zeng Z., Li X., Liu Y., Huang F. and Yu H. M. (2019) High-Precision Barium Isotope Measurements of Carbonates by MC-ICP-MS. *Geostand. Geoanalytical Res.* **43**, 291–300.

Table 1. Calculated values of average Ba-O/Cl bond length, coordination number (CN), force constant, and $10^3 \ln\beta$ of $^{137}Ba/^{134}Ba$ at 300 K.

Minerals	Calculated Ba-O/Cl (Å)	CN	Experimental Ba-O/Cl (Å)	Force constant <F> (N/m)	$10^3 \ln\beta$ (‰) at 300 K
Barite ($BaSO_4$)	2.9313	10	2.8785 (ref. 1)	73.5	0.55
Witherite ($BaCO_3$)	2.8504	9	2.8016 (ref. 2)	90.7	0.70
Aragonite_1/32 ($BaCa_{31}C_{32}O_{96}$)	2.7394	9	-	141.8	1.09
Aragonite_1/48 ($BaCa_{47}C_{48}O_{144}$)	2.7398	9	-	142.0	1.09
Calcite_1/24 ($BaCa_{23}C_{24}O_{72}$)	2.6694	6	-	112.3	0.85
Calcite_1/48 ($BaCa_{47}C_{48}O_{144}$)	2.6686	6	-	112.9	0.86
$BaCl_2$	3.1891	7	3.1595 (ref. 3)	58.6	0.46
$Ba(NO_3)_2$	2.9612	12	2.9101 (ref. 4)	77.0	0.59
$Ba(PO_3)_2$	2.8986	9	2.8871 (ref. 5)	81.2	0.63
$Ba_3(PO_4)_2$_Ba1	3.0318	12	2.9754 (ref. 6)	87.0	-
$Ba_3(PO_4)_2$_Ba2	2.8984	10	2.8342 (ref. 6)	90.1	-
$^*Ba_3(PO_4)_2$	2.9429	10.7	2.8813 (ref. 6)	89.1	0.69
$BaHPO_4$_Ba1	2.8746	9	2.8480 (ref. 7)	85.7	-
$BaHPO_4$_Ba2	2.9521	10	2.9195 (ref. 7)	71.3	-
$^*BaHPO_4$	2.9263	9.7	2.8957 (ref. 7)	76.1	0.58
$Ba(H_2PO_4)_2$	2.8323	8	2.7825 (ref. 8)	84.8	0.65
$Ba(OH)_2H_2O$	2.8591	8	2.8220 (ref. 9)	93.6	0.72
$Ba(OH)_2(H_2O)_3$	2.8646	8	2.8212 (ref. 10)	87.5	0.67
$Ba(OH)_2(H_2O)_8$	2.8383	8	2.7787 (ref. 11)	92.2	0.70
Aqueous Ba^{2+}	-	~8	-	90.5	0.72

The average Ba-O/Cl bond length and coordination number depend on the cutoff value used for Ba-O/Cl bond lengths. Here we adopted the cutoff of 3.3 Å for the calculations of average bond lengths and CNs. $^*Ba_3(PO_4)_2$ and $BaHPO_4$ have two types of Ba atoms and the Ba1:Ba2 ratios are 1:2 and 2:1 in $Ba_3(PO_4)_2$ and $BaHPO_4$, respectively. Experimental data: ref. 1, Miynre et al. (1978); ref. 2, Antao and Hassan (2007); ref. 3, Hull et al. (2011); ref. 4, Nowotny and Heger (1983); ref. 5, Grenier et al. (1967); ref.

6, Manoun et al. (2003); ref. 7, BenChaabane et al. (2004); ref. 8, Prelesnik et al. (1978); ref. 9, Kuske et al. (1988); ref. 10, Lutz et al. (1990); ref. 11, Persson et al. (1995).

Table 2. Polynomial fitting parameters of the reduced partition function ratios ($10^3 \ln\beta$) of $^{137}Ba/^{134}Ba$ with temperature for all minerals and aqueous Ba^{2+}.

Minerals	a	b	c
Barite ($BaSO_4$)	0.0507	-1.1653E-04	1.9119E-06
Witherite ($BaCO_3$)	0.0638	-1.4915E-04	2.9151E-06
Aragonite_1/32 ($BaCa_{31}C_{32}O_{96}$)	0.1004	-2.6551E-04	3.8841E-06
Aragonite_1/48 ($BaCa_{47}C_{48}O_{144}$)	0.1006	-2.7008E-04	3.9698E-06
Calcite_1/24 ($BaCa_{23}C_{24}O_{72}$)	0.0790	-2.5029E-04	3.6254E-06
Calcite_1/48 ($BaCa_{47}C_{48}O_{144}$)	0.0798	-2.5963E-04	3.7316E-06
$BaCl_2$	0.0421	-2.1989E-05	2.3485E-08
$Ba(NO_3)_2$	0.0544	-1.3683E-04	2.8937E-06
$Ba(PO_3)_2$	0.0575	-1.3110E-04	1.8372E-06
$Ba_3(PO_4)_2$	0.0634	-1.2212E-04	1.6007E-06
$BaHPO_4$	0.0540	-1.6108E-04	3.0692E-06
$Ba(H_2PO_4)_2$	0.0602	-1.8401E-04	3.4898E-06
$Ba(OH)_2H_2O$	0.0666	-1.7719E-04	2.7304E-06
$Ba(OH)_2(H_2O)_3$	0.0621	-2.6802E-04	5.9002E-06
$Ba(OH)_2(H_2O)_8$	0.0651	-2.7512E-04	5.5999E-06
Aqueous Ba^{2+}	0.0649	0	0

Polynomial fitting equation: $10^3 \ln\beta = a*x + b*x^2 + c*x^3$, where $x = 10^6/T^2$ and T is temperature in Kelvin. All polynomial fittings are performed between 250 K and 2500 K.

Table 3. Polynomial fitting parameters of the equilibrium Ba isotope fractionation factors ($10^3 \ln\alpha$) of $^{137}Ba/^{134}Ba$ between minerals and aqueous Ba^{2+}.

Minerals	a	b	c
Barite ($BaSO_4$)	-0.0142	-1.1653E-04	1.9119E-06
Witherite ($BaCO_3$)	-0.0011	-1.4915E-04	2.9151E-06
Aragonite_1/32 ($BaCa_{31}C_{32}O_{96}$)	0.0355	-2.6551E-04	3.8841E-06
Aragonite_1/48 ($BaCa_{47}C_{48}O_{144}$)	0.0357	-2.7008E-04	3.9698E-06
Calcite_1/24 ($BaCa_{23}C_{24}O_{72}$)	0.0141	-2.5029E-04	3.6254E-06
Calcite_1/48 ($BaCa_{47}C_{48}O_{144}$)	0.0149	-2.5963E-04	3.7316E-06
$BaCl_2$	-0.0228	-2.1989E-05	2.3485E-08
$Ba(NO_3)_2$	-0.0105	-1.3683E-04	2.8937E-06
$Ba(PO_3)_2$	-0.0074	-1.3110E-04	1.8372E-06
$Ba_3(PO_4)_2$	-0.0015	-1.2212E-04	1.6007E-06
$BaHPO_4$	-0.0109	-1.6108E-04	3.0692E-06
$Ba(H_2PO_4)_2$	-0.0047	-1.8401E-04	3.4898E-06
$Ba(OH)_2H_2O$	0.0017	-1.7719E-04	2.7304E-06
$Ba(OH)_2(H_2O)_3$	-0.0028	-2.6802E-04	5.9002E-06
$Ba(OH)_2(H_2O)_8$	0.0002	-2.7512E-04	5.5999E-06

Polynomial fitting equation: $10^3 \ln\alpha = a*x + b*x^2 + c*x^3$, where $x = 10^6/T^2$ and T is temperature in Kelvin. All polynomial fittings are performed between 250 K and 2500 K.

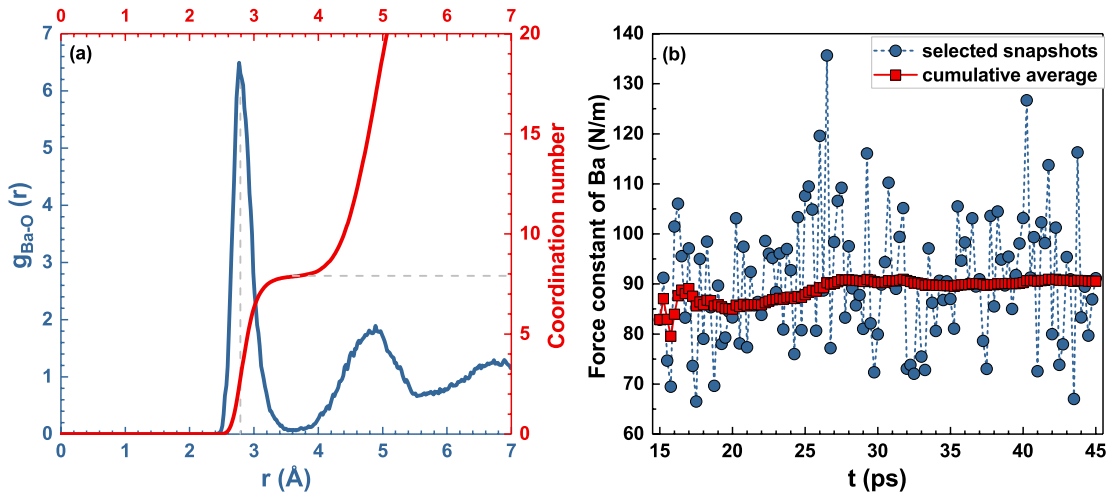

Figure 1. (a) Radial distribution functions g(r) for Ba-O pair (blue line) and coordination number (CN) of aqueous Ba^{2+} (red line). (b) The force constants of Ba atom in the selected snapshots from the first-principles molecular dynamic simulation (blue points) and their cumulative averages in the time domain (red points).

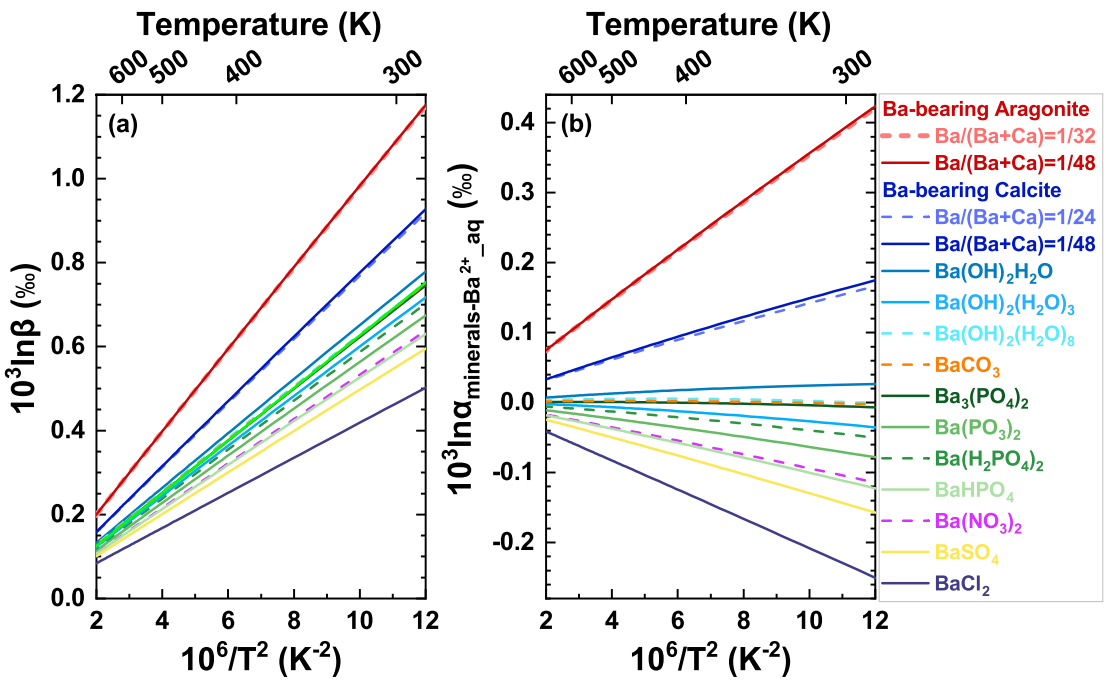

Figure 2. (a) The reduced partition function ratios ($10^3\ln\beta$) of $^{137}Ba/^{134}Ba$ of minerals as a function of temperature. (b) The equilibrium Ba isotope fractionation ($10^3\ln\alpha$) between minerals and aqueous Ba^{2+}. The $10^3\ln\beta$ of aqueous Ba^{2+} is derived from the average force constant of snapshots obtained from the first-principles molecular dynamic simulation. The validity of this approach will be discussed in section 3.3.

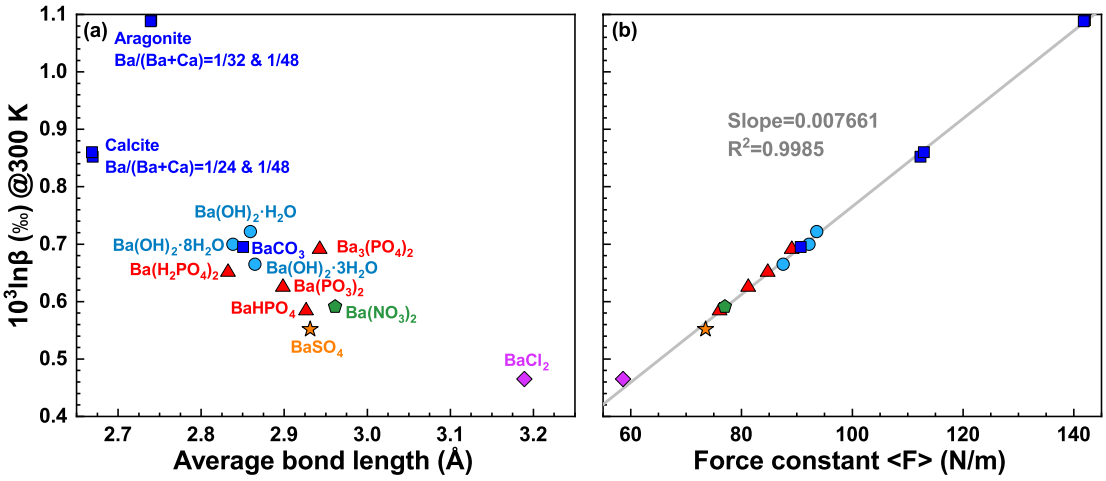

Figure 3. The $10^3 \ln\beta$ of $^{137}Ba/^{134}Ba$ at 300 K versus (a) the average Ba-O/Cl bond length in all investigated minerals (b) the force constant. Blue squares, cyan circles, red triangles, green pentagon, orange star, and purple diamond refer to carbonates, barium hydroxide polyhydrates, phosphates, nitrate ($BaNO_3$), barite, and $BaCl_2$, respectively.

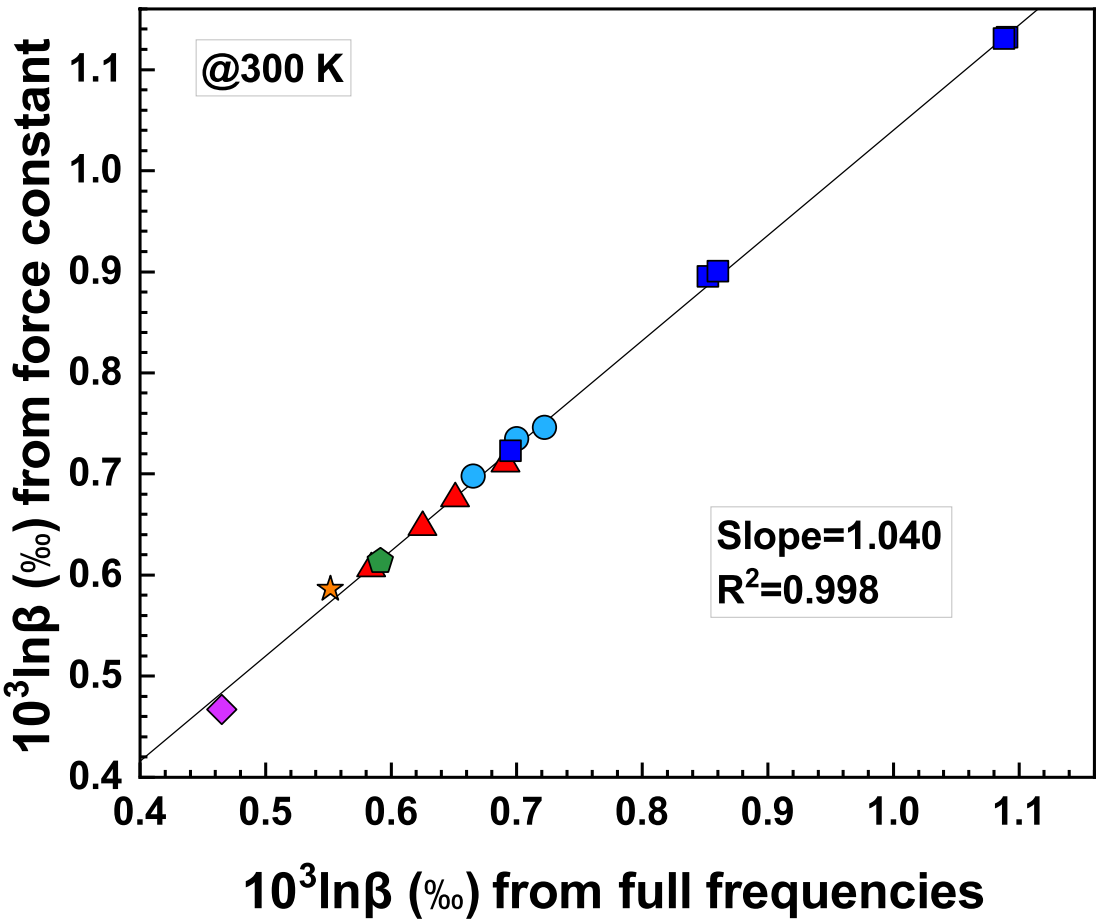

Figure 4. Comparison of mineral $10^3 \ln\beta$ values calculated from full frequencies (Urey equation) with those calculated from force constants. The slope of the linear fitting is 1.040 with a coefficient of determination (R^2) of 0.998, suggesting that the systematic deviation between Eq. (7) and Eq. (1) is about 4%.

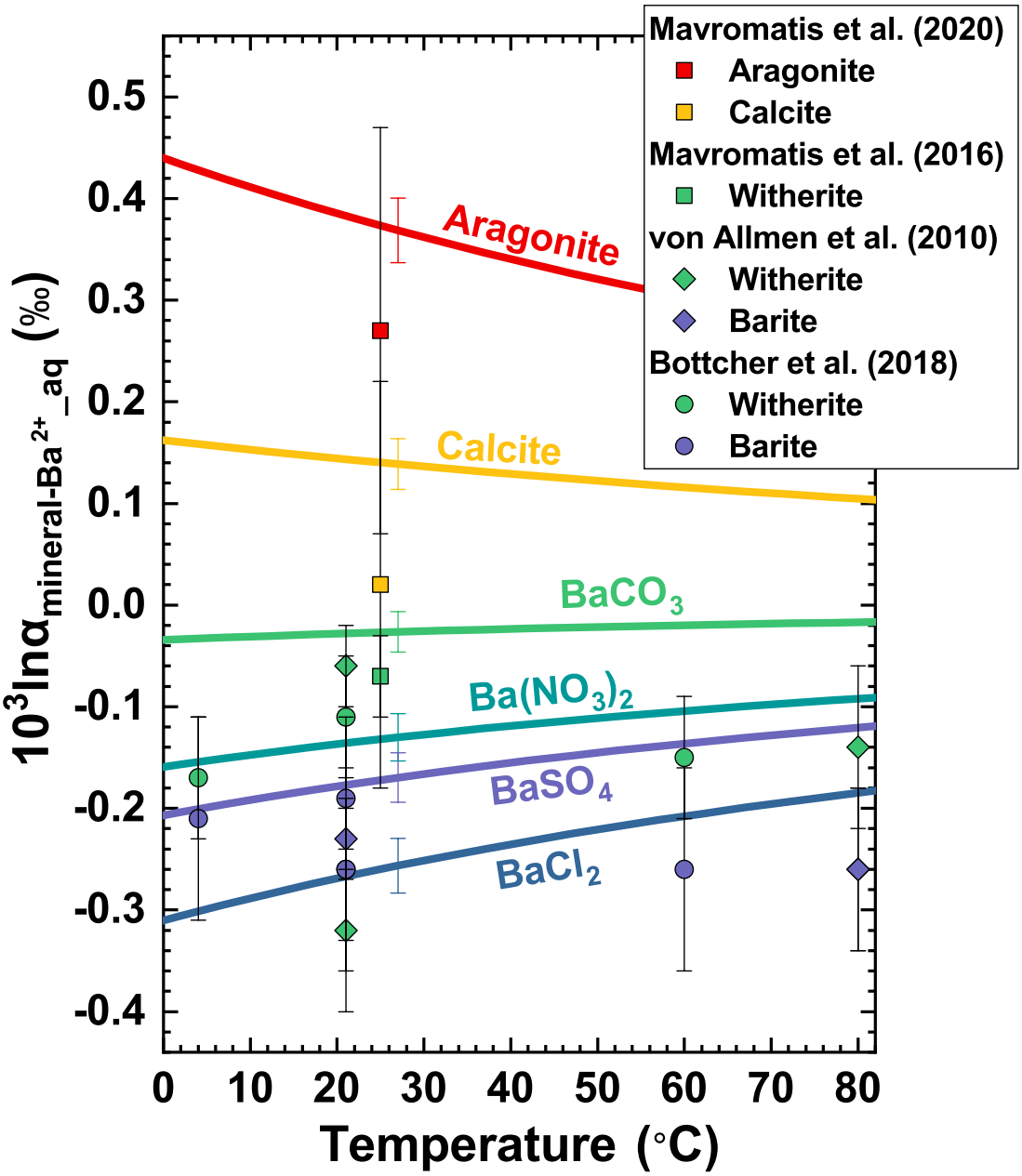

Figure 5. The equilibrium Ba isotope fractionation factors ($10^3 \ln\alpha$) of $^{137}Ba/^{134}Ba$ between some minerals and aqueous Ba^{2+} as a function of temperature. Lines represent the calculated results in this study and scattered points are experimental results from previous studies (von Allmen et al., 2010; Mavromatis et al., 2016; Böttcher et al., 2018; Mavromatis et al., 2020).

Supplementary materials

Table S1. The *k*-point grid used for electronic integrations over the Brillouin zone and the supercell size used for calculating the phonon frequencies.

Minerals	*k*-point grid	Supercell size
Barite ($BaSO_4$)	4×6×4	2×2×2
Witherite ($BaCO_3$)	8×6×8	2×2×2
Aragonite_1/32 ($BaCa_{31}C_{32}O_{96}$)	1×1×1	1×1×1
Aragonite_1/48 ($BaCa_{47}C_{48}O_{144}$)	1×1×1	1×1×1
Calcite_1/24 ($BaCa_{23}C_{24}O_{72}$)	2×2×1	1×1×1
Calcite_1/48 ($BaCa_{47}C_{48}O_{144}$)	1×1×1	1×1×1
$BaCl_2$	8×12×6	2×2×2
$Ba(NO_3)_2$	6×6×6	2×2×1
$Ba(PO_3)_2$	4×4×4	1×2×2
$Ba_3(PO_4)_2$	8×8×8	2×2×2
$BaHPO_4$	4×1×1	2×1×1
$Ba(H_2PO_4)_2$	4×4×4	1×2×1
$Ba(OH)_2H_2O$	12×6×6	2×2×2
$Ba(OH)_2(H_2O)_3$	6×4×8	2×1×2
$Ba(OH)_2(H_2O)_8$	2×2×2	1×1×1

Table S2. The calculated cell parameters and volumes of minerals compared with experimental data.

Minerals	a (Å)	b (Å)	c (Å)	α (°)	β (°)	γ (°)	Volume (Å^3)	
Barite ($BaSO_4$)	9.0272	5.5636	7.2752	90	90	90	365.3857	This study
	7.1570	8.8840	5.4570	90	90	90	346.9713	ref. 1
Witherite ($BaCO_3$)	5.3731	8.9969	6.5925	90	90	90	318.6918	This study
	5.3103	8.9122	6.4365	90	90	90	304.6167	ref. 2
Aragonite_1/32 ($BaCa_{31}C_{32}O_{96}$)	10.0663	16.0769	11.6839	89.88	90	90	1890.8522	This study
Aragonite_1/48 ($BaCa_{47}C_{48}O_{144}$)	15.0606	16.0765	11.6608	89.93	90	90	2823.3368	This study
Calcite_1/24 ($BaCa_{23}C_{24}O_{72}$)	10.1243	10.1243	17.3626	90.00	90.00	120.00	1541.2400	This study
Calcite_1/48 ($BaCa_{47}C_{48}O_{144}$)	10.1154	10.1154	34.5327	90	90	120	3060.0290	This study
$BaCl_2$	7.9985	4.8344	9.5727	90	90	90	370.1535	This study
	7.8813	4.7369	9.4360	90	90	90	352.2735	ref. 3
$Ba(NO_3)_2$	8.2791	8.2791	8.2791	90	90	90	567.4753	This study
	8.1184	8.1184	8.1184	90	90	90	535.0708	ref. 4
$Ba(PO_3)_2$	9.8668	6.9781	7.6790	90	94.57	90	527.0400	This study
	9.6950	6.9060	7.5220	90	94.75	90	501.8958	ref. 5
$Ba_3(PO_4)_2$	5.6854	5.6854	21.3533	90	90	120	597.7589	This study
	5.6046	5.6046	21.0010	90	90	120	571.2942	ref. 6
$BaHPO_4$	4.6404	14.3711	17.4037	90	90	90	1160.6241	This study
	4.6090	14.1950	17.2140	90	90	90	1126.2217	ref. 7
$Ba(H_2PO_4)_2$	10.8184	7.7425	8.6704	90	90	90	726.2433	This study
	10.2420	7.7930	8.5600	90	90	90	683.2242	ref. 8
$Ba(OH)_2H_2O$	3.9402	6.4062	7.0500	90	90	90	177.9538	This study
	3.8947	6.3657	6.9523	90	90	90	172.3648	ref. 9
$Ba(OH)_2(H_2O)_3$	7.6196	11.4562	6.0284	90	90	90	526.2317	This study
	7.6400	11.4030	5.9650	90	90	90	519.6644	ref. 10
$Ba(OH)_2(H_2O)_8$	9.2874	9.2779	11.8092	90	99.23	90	1004.3950	This study
	9.301	9.289	11.848	90	98.94	90	1011.19593	ref. 11

Experimental data: ref. 1, Miynre et al. (1978); ref. 2, Antao and Hassan (2007); ref. 3, Hull et al. (2011); ref. 4, Nowotny and Heger (1983); ref. 5, Grenier et al. (1967); ref. 6, Manoun et al. (2003); ref. 7, BenChaabane et al. (2004); ref. 8, Prelesnik et al. (1978); ref. 9, Kuske et al. (1988); ref. 10, Lutz et al. (1990); ref. 11, Persson et al. (1995).

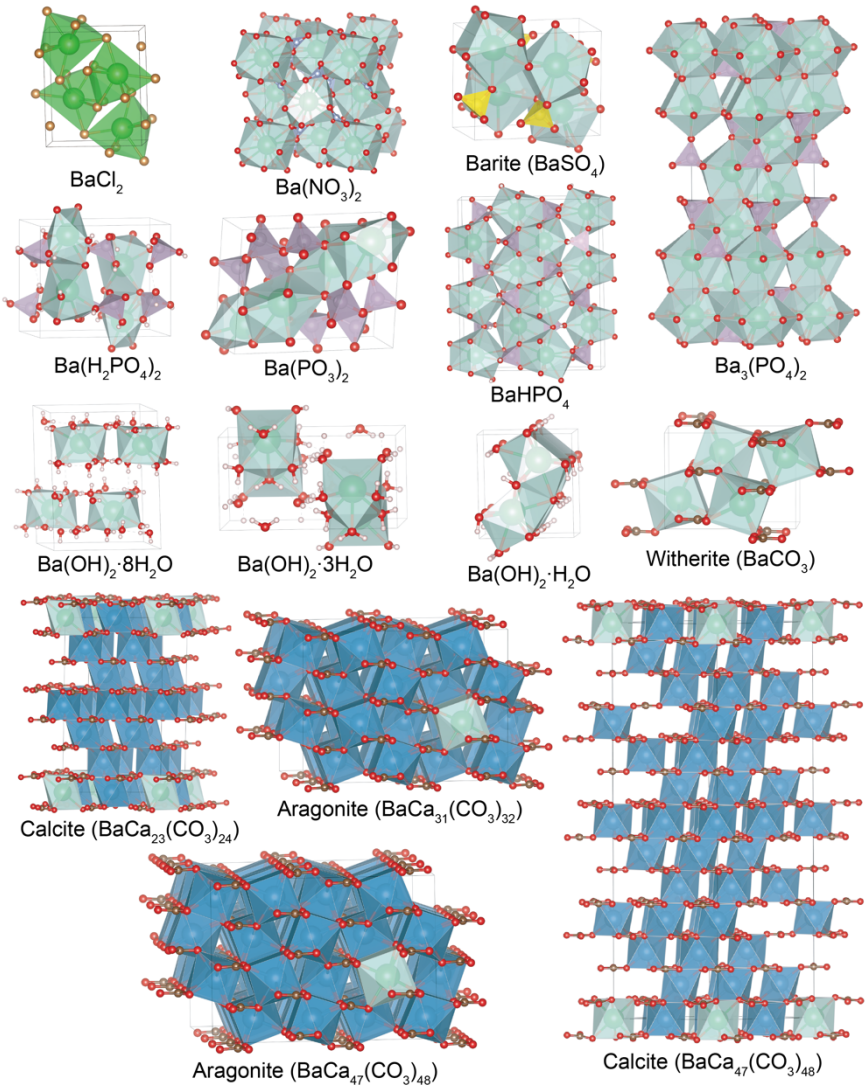

Figure S1. Relaxed structures of minerals investigated in this study. The Ba-O and Ba-Cl polyhedrons are colored with light cyan and green. The dark blue represents Ca-O polyhedrons.

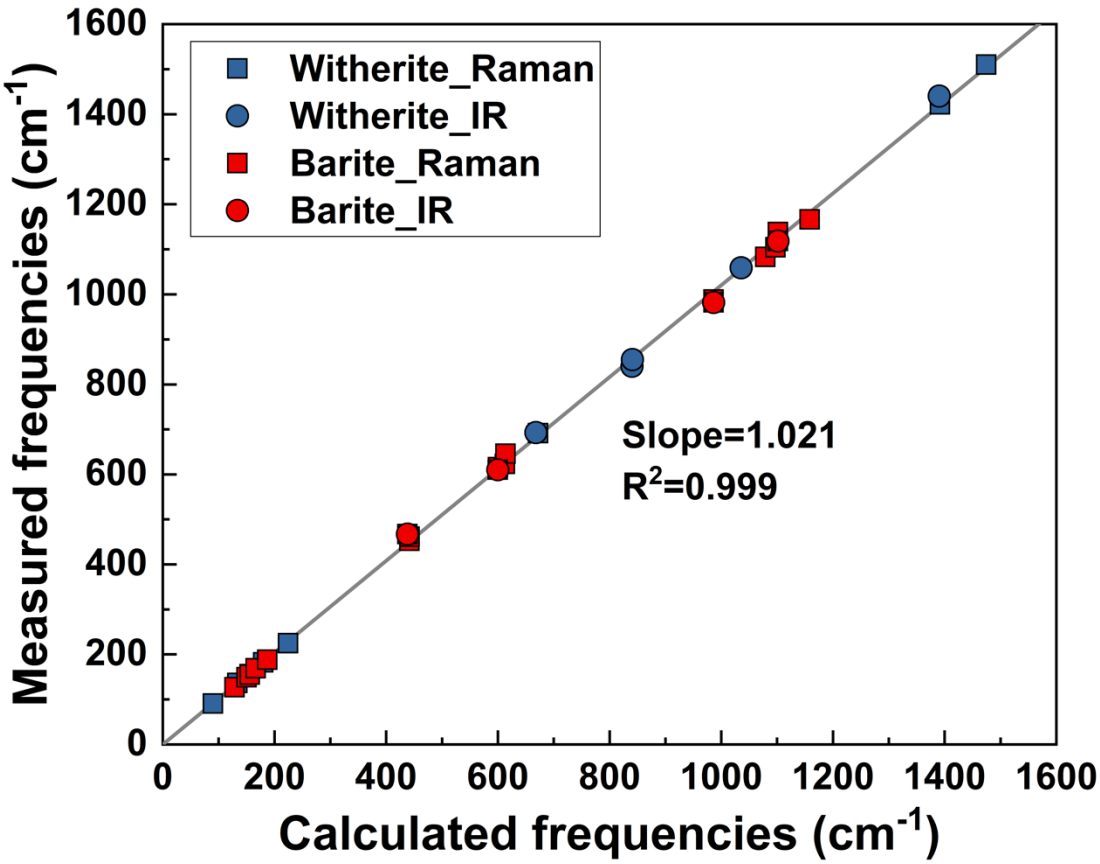

Figure S2. Comparison of vibrational frequencies of witherite ($BaCO_3$) and barite ($BaSO_4$) between the DFT calculations in this study and previous experimental results. Experimental data: Raman spectra for witherite (Wang et al., 2019) and barite (Zhou et al., 2020); Infrared spectra for witherite (Chaney et al., 2015; Wang et al., 2019) and barite (Dimova et al., 2006; Lane, 2007).

References

Antao S. M. and Hassan I. (2007) BaCO3: high-temperature crystal structures and the Pmcn→R3m phase transition at 811°C. *Phys. Chem. Miner.* **34**, 573–580. Available at: http://link.springer.com/10.1007/s00269-007-0172-8.

BenChaabane T., Smiri L. and Bulou A. (2004) Vibrational study and crystal structure refinement of BaHPO4. *Solid State Sci.* **6**, 197–204. Available at: https://linkinghub.elsevier.com/retrieve/pii/S1293255803002577.

Chaney J., Santillán J. D., Knittle E. and Williams Q. (2015) A high-pressure infrared and Raman spectroscopic study of BaCO3: the aragonite, trigonal and Pmmn structures. *Phys. Chem. Miner.* **42**, 83–93. Available at: http://link.springer.com/10.1007/s00269-014-0702-0.

Dimova M., Panczer G. and Gaft M. (2006) Spectroscopic study of barite from the Kremikovtsi Deposit (Bulgaria) with implication for its origin. *Geol. Anal. Balk. poluostrva*, 101–108. Available at: http://www.doiserbia.nb.rs/Article.aspx?ID=0350-06080667101D.

Grenier J.-C., Martin C., Durif-Varambon A., Tranqui D. and Guitel J.-C. (1967) Une nouvelle forme du métaphosphate de baryum Ba(PO3)2. *Bull. la Société française Minéralogie Cristallogr.* **90**, 24–31. Available at: https://www.persee.fr/doc/bulmi_0037-9328_1967_num_90_1_6062.

Hull S., Norberg S. T., Ahmed I., Eriksson S. G. and Mohn C. E. (2011) High temperature crystal structures and superionic properties of SrCl2, SrBr2, BaCl2 and BaBr2. *J. Solid State Chem.* **184**, 2925–2935. Available at: https://linkinghub.elsevier.com/retrieve/pii/S0022459611004865.

Kuske P., Engelen B., Henning J., Lutz H. D., Fuess H. and Gregson D. (1988) Neutron diffraction study of Sr(OH)2 · H2O and β-Ba(OH)2 · H20. *Zeitschrift für Krist. - Cryst. Mater.* **183**. Available at: http://www.degruyter.com/view/j/zkri.1988.183.issue-1-4/zkri.1988.183.14.319/zkri.1988.183.14.319.xml.

Lane M. D. (2007) Mid-infrared emission spectroscopy of sulfate and sulfate-bearing minerals. *Am. Mineral.* **92**, 1–18. Available at: https://pubs.geoscienceworld.org/ammin/article/92/1/1-18/134286.

Lutz H. D., Kellersohn T. and Vogt T. (1990) Hydrogen bonding in barium hydroxide trihydrate by neutron diffraction. *Acta Crystallogr. Sect. C Cryst. Struct. Commun.* **46**, 361–363. Available at: http://scripts.iucr.org/cgi-bin/paper?S0108270189006761.

Manoun B., Popović L., De Waal D. and Verryn S. M. C. (2003) Rietveld refinements of a new solid solution Ba (3− x) Sr x (PO 4) 2 (0≤ x ≤3). *Powder Diffr.* **18**, 122–127. Available at: https://www.cambridge.org/core/product/identifier/S0885715600007636/type/journal_article.

Miynre M., Minero I. and Ssrn-rcur H. M. (1978) Crystal structures and sulphate force constants ofbarite, celestite, and anglesite. *Phys. Chem. Miner.* **63**, 506–510.

Nowotny H. and Heger G. (1983) Structure refinement of strontium nitrate, Sr(NO3)2, and barium nitrate, Ba(NO3)2. *Acta Crystallogr. Sect. C Cryst. Struct. Commun.*

39, 952–956. Available at: http://scripts.iucr.org/cgi-bin/paper?S0108270183006976.

Persson I., Sandström M. and Yokoyama H. (1995) Structure of the Solvated Strontium and Barium Ions in Aqueous, Dimethyl Sulfoxide and Pyridine Solution, and Crystal Structure of Strontium and Barium Hydroxide Octahydrate. *Zeitschrift für Naturforsch. A* **50**, 287. Available at: https://www.degruyter.com/view/j/zna.1995.50.issue-1/zna-1995-0105/zna-1995-0105.xml.

Prelesnik B., Herak R., Čurić M. and Krstanović I. (1978) The crystal structure of orthorhombic barium dihydrogenphosphate. *Acta Crystallogr. Sect. B* **34**, 76–78. Available at: http://scripts.iucr.org/cgi-bin/paper?S0567740878002320.

Wang X., Ye Y., Wu X., Smyth J. R., Yang Y., Zhang Z. and Wang Z. (2019) High-temperature Raman and FTIR study of aragonite-group carbonates. *Phys. Chem. Miner.* **46**, 51–62. Available at: http://dx.doi.org/10.1007/s00269-018-0986-6.

Zhou L., Mernagh T. P., Mo B., Wang L., Zhang S. and Wang C. (2020) Raman Study of Barite and Celestine at Various Temperatures. *Minerals* **10**, 260. Available at: https://www.mdpi.com/2075-163X/10/3/260.